UNIVERSITAT POLITÈCNICA DE VALÈNCIA

Escuela Técnica Superior de Ingeniería del Diseño

# AERONAUTICS AND AEROSPACE DEPARTMENT

## von KARMAN INSTITUTE FOR FLUID DYNAMICS

# Photogrammetry Reconstruction of Plasma Wind Tunnel Sample

AUTHOR: JOSÉ ANTONIO MARÍN GARCÍA

SUPERVISOR VKI: OLIVIER CHAZOT

ADVISOR VKI: BERND HELBER
ADVISOR VKI: FRANCISCO TORRES HERRADOR

SUPERVISOR UPV: ISRAEL QUINTANILLA GARCÍA
ADVISOR UPV: JOSÉ LUIS LERMA GARCÍA

September, 2019

*Dedicado a*
*mi familia*

# Summary

During space missions, the thermal protection systems (TPS) of space vehicles play a crucial role during the atmospheric entry stage. Due to the blunt shape of these bodies and the hypersonic flight speeds, a separate shock wave is formed and behind that, the high temperatures (10000K) that are typically reached pose a major problem for the structural integrity of the vehicle. Ablative materials allow thermal protection of the structure through physico-chemical decomposition in a process known as ablation. To characterize these materials, the "von Karman Institute for Fluid Dynamics" has the most powerful inductive plasma wind tunnel in the world: the VKI Plasmatron. This wind tunnel can generate plasma characteristic from an atmospheric entry. Currently, the ablation speed (recession) of the material is studied with a high-speed camera located perpendicular to the sample, but it is only possible to obtain one- or two-dimensional results. It has been investigated if the use of stereo photogrammetry, using two cameras, would allow to reconstruct the evolution of the surface in 3 dimensions of a type test sample used in the VKI Plasmatron. In this work, we study how the position of the cameras, their different parameters and calibration methods affect the reconstruction of the sample. For this, the Stereo 3D reconstruction code initially developed by G. Martínez (TFM 2018) and improved by S. Cantos (TFM 2019) has been used. The angle formed by the cameras is an important parameter in the reconstruction of the surface, so the reduced visual accessibility in the VKI Plasmatron poses a challenge to find an optimal configuration. In addition, due to the high brightness conditions induced by the plasma, the cameras must be configured and adapted to avoid over-exposure and, therefore, the loss of information in the images. Likewise, it has been observed that the calibration method using a 3D pattern implies greater flexibility to perform the reconstruction of other objects. The photogrammetric system developed in this project represents an advance for the study of ablative materials in the VKI through an economic and simple system for the end user. This will allow to know the state of the entire surface exposed to the plasma without the assumption symmetries.

**Keywords:** atmospheric entry, ablation, plasma wind tunnel, stereo photogrammetry, 3D reconstruction.

# Resumen

Durante las misiones espaciales, los sistemas de protección térmica (TPS) de los vehículos espaciales juegan un papel crucial durante la etapa de entrada atmosférica. Debido a la forma roma de estos cuerpos y a las velocidades de vuelo hipersónico, se forma una onda de choque separada que tras ella las altas temperaturas (10000K) que se alcanzan suponen un gran problema para la integridad estructural del vehículo. Los materiales ablativos permiten la protección térmica de la estructura a través de la descomposición química y de sacrificio de material (proceso conocido como ablación). Para caracterizar estos materiales el "von Karman Institute for Fluid Dynamics" cuenta con el túnel de viento de plasma de tipo inductivo más potente del mundo: el VKI Plasmatron. Este túnel de viento es capaz de generar plasma característico de una entrada atmosférica. Actualmente, la ablación del material se estudia con una cámara de alta velocidad situada de forma perpendicular a la muestra, pero únicamente es posible obtener resultados unidimensionales y bidimensionales. Se ha investigado si la utilización de estéreo fotogrametría, utilizando dos cámaras, permite reconstruir la evolución de la superficie en 3 dimensiones de una probeta tipo utilizada en el VKI Plasmatron. En este trabajo, se estudia cómo la posición de las cámaras, sus diferentes parámetros y métodos de calibración afectan a la reconstrucción de la probeta. Para ello, se ha utilizado el código Stereo 3D reconstruction desarrollado inicialmente por G. Martínez (TFM 2018) y mejorado por S. Cantos (TFM 2019). El ángulo que forman las cámaras es un parámetro muy importante a la hora de reconstruir una superficie, por lo que la accesibilidad visual tan reducida en el VKI Plasmatron supone un gran problema a la hora de encontrar una configuración óptima. Además, debido a las condiciones de alta luminosidad inducidas por el plasma, las cámaras deben ser configuradas y adaptadas para evitar la sobreexposición y, por tanto, la pérdida de información en las imágenes. Asimismo, se ha observado que el método de calibración mediante un patrón 3D supone una mayor flexibilidad para realizar la reconstrucción de otros objetos. El sistema fotogramétrico desarrollado en este proyecto supone un avance para el estudio de materiales ablativos en el VKI mediante un sistema económico y simple para el usuario final. Esto permitirá conocer el estado de toda la superficie expuesta al plasma sin asumir simetrías.

**Palabras clave:** reentrada atmosférica, ablación, túnel de viento de plasma, estéreo fotogrametría, reconstrucción 3D.

# Contents

# List of Figures

# List of Tables

# Nomenclature

## Acronyms

CCD  Charge Coupled Device

CCP  Commercial Crew Program

CMOS  Complementary Metal Oxide Semiconductor

CTE  Coefficient of Thermal Expansion

ICP    Induction Coupled Plasma

LEO  Low Earth Orbit

MSE  Mean Square Error

OpenCV  Open Computer Vision

RANSAC  Random Sample Consensus

ROI    Region of Interest

SIFT  Scale-Invariant Feature Transformation

TPM  Thermal Protection Material

TPS   Thermal Protection System

## Subscript

*corrected*  variable after correcting the radial or tangential distortion

$l$        left

$r$       right

$x$       horizontal axis direction

$y$       vertical axis direction

## Superscript

*calib*  calculated by a mathematical function of CAD design

*left*  left camera

*right*  right camera

*simul*  calculated by the reconstruction code

## Symbols

$\Pi$  Projective plane

$c$  Center of the image

$d$  Disparity

$e$  Epipole located on the image plane

$F$  Physical focal length

$f$  Focal length of the camera

$k$  Terms of a Taylor expansion for radial distortion correction

$O$  Center of projection of the camera

$P$  Point in real world

$p$  Points onthe imagin plane

$p$  Terms of a Taylor expansion for tangential distortion correction

$s$  Size of the individual imager elements

$T$  Distance between cameras

$X$  Length of the object in horizontal direction (world coordinates)

$x$  Horizontal length coordinate of the object projected on the imaging plane (screen coordinates)

$Y$  Length of the object in vertical direction (world coordinates)

$y$  Vertical length coordinate of the object projected on the imaging plane (screen coordinates)

$Z$  Distance from the camera to the object (depth)

$E$  Essential matrix

F       Fundamental matrix

H       Horizontal direction

M       Camera intrinsic matrix

np      Number of points in the reconstruction mesh

Q       Homogeneous vector of physical world points in camera coordinates

q       Homogeneous vector of camera coordinates

R       Rotation

T       Translation

V       Vertical direction

# Chapter 1

# Introduction

Atmospheric entry is crucial in future space transportation, including planetary exploration, crew and cargo transportation, next-generation launchers, space planes and sample-return missions. During (re)-entry missions of the spacecraft in the atmosphere at hypersonic velocities, a detached shock wave is generated around the blunt body (Figure 1.1). This increases the temperature of the flow up to $10\,000\,\mathrm{K}$ [1]. The importance to properly design the Thermal Protection System (TPS) is essential to carry out a successful mission and safeguard the vehicle payload.
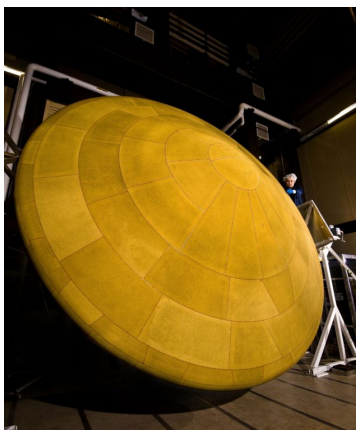


(a) Space heatshield [2].   (b) Simulation of re-entry [3]
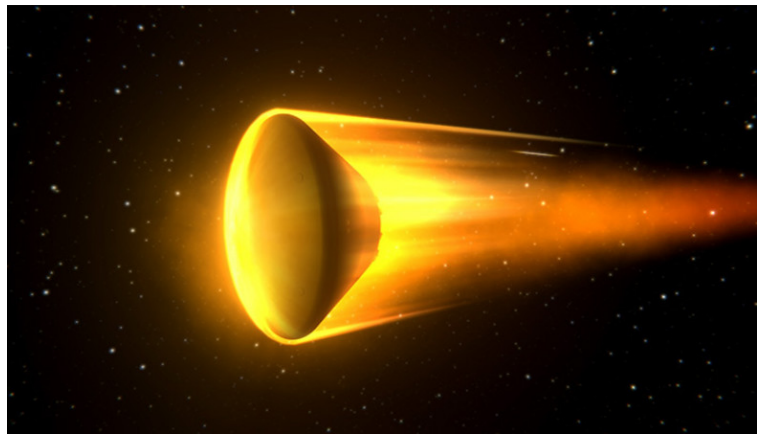
Figure 1.1: Space heatshield that illustrates the blunt body shape and the atmosphere re-entry situation.

Most ablative materials are composed of a rigid precursor and a filling matrix. The main purpose of this material composition is the dissipation of high heat fluxes through physical and chemical decomposition. They transform the thermal energy into mass loss and surface recession, while the remaining solid material protects the vehicle substructure.

In 1969, Goddard's idea about ablative TPS allowed the first humans to safely return to Earth at a speed of 11.2 km/s after landing on the Moon aboard the Apollo 11 Lunar Module [4]. After identify, develop, and qualify required technologies for sample return missions from Mars or asteroids to Earth, in the future sample return missions, this type of materials will allow re-entry speeds exceeding 14 km/s. These re-entry speeds are associated with a module returning to Earth after a mission. However, the Galileo Probe deceleration module experimented the most severe heating environment when it entered the atmosphere of Jupiter at a relative velocity 47.4 km/s on 1995 [5].

In order to increase the payload, a new class of lightweight carbon-phenolic composites has been developed. The thickness of the TPS is an important design parameter to determine but it depends on the heat flux to spacecraft and this value is difficult to estimate with high precision, thus high safety margins are currently used. Ground tests in plasma wind-tunnels are the only affordable possibility for material qualification and validation material response code to determine the TPS thickness. In this project, the VKI Plasmatron has been used to reproduce the aerothermodynamic environment of re-entry plasma flows. (Figure 1.2)
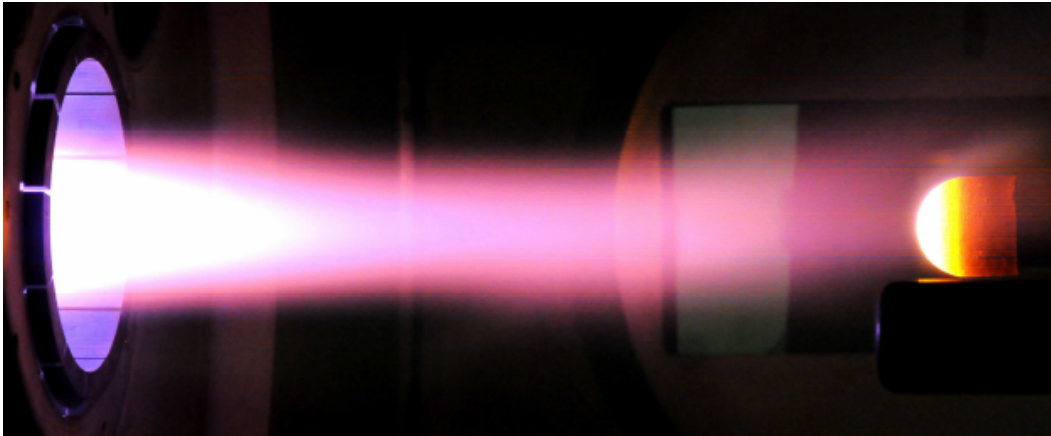


Figure 1.2: VKI Plasmatron during an ablation experiment. [1]

To measure and characterize the surface recession of these ablative materials, it is necessary to develop a visual technique installed on the visual accesses of the facility VKI Plasmatron. Currently, at Von Karman Institute (VKI) a high speed camera is used to record an image orthogonal to the plasma but this method allows only one-dimensional (1D) and two-dimensional (2D) measurements (Figure 1.3). In this project, a new technique based on stereo photogrammetry reconstruction will be developed to characterize the surface recession of the ablative TPS three-dimensionally (3D) by pictures taken from two cameras placed in two different sides. While not much literature on photogrammetry for heat-shield characterization are found [6, 7]), other fields such

topography and cartography are a great source of information [8, 9].
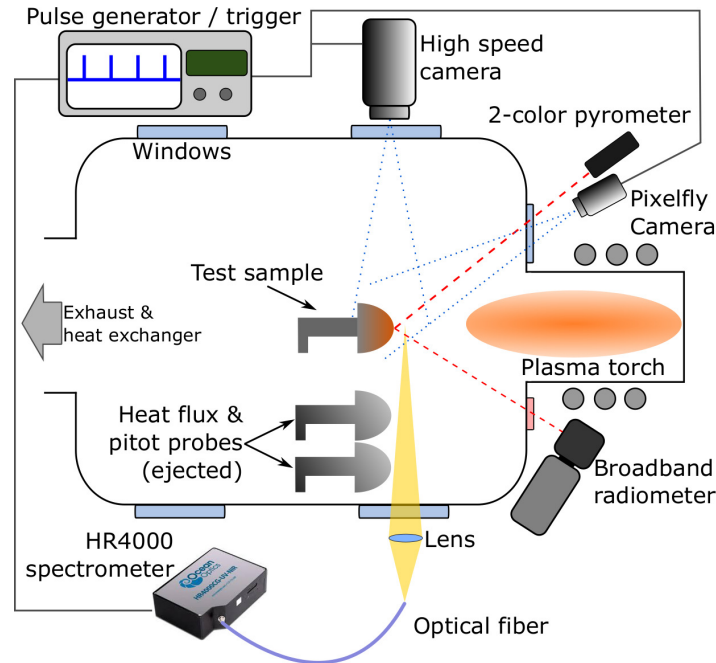


Figure 1.3: Scheme of the current ablation experiments using the high speed camera. Courtesy of Francisco Torres.

This technique has been implemented in a previous work at VKI [10] in which a preliminary stereo photogrammetry reconstruction of the test sample, apart from the test bench, was done. The result is a 3D model of the sample made from an open source code developed in Python using the Open CV library.

## 1.1 Research Objectives and Methodology

The objectives to reach in this project are:

- Develop an experimental procedure to characterize the sample surface recession along the ablation experiments carried out at the VKI Plasmatron by stereo photogrammetry 3D reconstruction.

- Develop an experimental methodology to take pictures of the sample dealing with the high brightness conditions during the tests and taking into account the visual limitation from the windows of the plasma wind tunnel facility.

- Calibrate the cameras using a known geometry 3D model to obtain the optimum input parameters of the reconstruction code and use them to reconstruct a similar geometry.

- Synchronize the cameras used for the photogrammetry reconstruction with the rest of the equipment and measuring devices working during the ablation experiments at VKI Plasmatron.

Regarding the methodology followed in this project, it consists in two parts. The first part consists of the preliminary study apart from the test bench. The second part consists of the experimental study on the test facility. Although, the first study is necessary to establish the best camera configuration, both tasks have been developed in parallel due to the availability of the VKI Plasmatron, the samples, other measuring devices, etc.

The first part includes triggering both cameras to take pictures synchronously. Also, find out the best camera configuration outside the VKI Plasmatron through a parametric study, to determine the angle and distance from cameras to the sample in order to reconstruct most of the sample. Then, using an optimization algorithm to find the best combination of the input parameters of the reconstruction code which minimize the Mean Square Error (MSE). Finally, perform a reconstruction of the sample.

The second part consists of figuring out the best camera arrangement on the VKI Plasmatron windows. There are other measuring devices placed on the windows and the space is limited. Then, it is necessary to set up the cameras to take pictures taking into account the brightness conditions depending on the heat flux. The purpose is to take pictures avoiding the loss of information of some parts of the sample if over saturated parts appears in the images taken. The final step is to make a reconstruction of the sample tested inside the VKI Plasmatron along the duration of the experiment.

# Chapter 2

# Literature Review

For better understanding of this project, three main topics are going to be presented: space heat shields, photogrammetry concept and photography concept. The space heat shields are the main motivation of the study because they are used for atmospheric entry missions. Photogrammetry is an alternative solution proposed to measure the surface recession of the ablative material instead of the high speed camera. Photography concepts in order get high quality pictures dealing with the measurement conditions. This is very important to avoid losing information in some pixels of the pictures and allowing the code to perform the reconstruction.

## 2.1 Space heat shield. Configuration and Characterization

When a spacecraft performs a critical operation like the re-entry form space to the atmosphere at high velocities (hypersonic flows), a detached shock wave is generated around the blunt body [11]. the high energy produced under the hypersonic velocities made necessary to research new ways to maintain the integrity of the spacecraft.

Ballistic missile designs supposed a great influence for the early development of Thermal Protection System (TPS). Based on the idea of the missile designs, the blunt body design arose. In slender bodies an oblique shock wave appears and causes high heating load on the structure. Unlike, blunt bodies deflect the heat from the kinetic energy away via a strong bow shock wave. However, in front of the vehicle, the surface still reaches several thousand Kelvin and there is no material that supports reentry speeds of 11 km/s, such as, the lunar return. Although meteors reach higher reentry speeds, the only way to withstand high thermal energy is through transformation and destruction of material.

With the Space Race in full swing, in the Apollo program in 1958 or Suyuz program

in 1966, the need for TPS able to withstand the return from lunar orbit arose. This TPS also should be able to protect from micrometeorites and orbital debris and withstand vacuum and ultraviolet exposure. To provide the protection needed, an ablative heat shield was used to endure the heat produced form lunar orbit reentry. An ablator dissipates heat by means of a thermal fusion shield, resulting in a single-use TPS system. Years later, the space shuttle presented a new type of TPS . As this vehicle would be entering from Low Earth Orbit (LEO) instead of lunar orbit, it needed a reusable and lightweight TPS, so new materials had to be considered based on carbon-phenolic materials which are the ones studied in this project.

When considering a new TPS design it is important to take into account the types that exist and the differences between them [12]. It is crucial in knowing what type is needed for different missions.

**Reusable TPS**. (Figure 2.1(a)). After exposure to the entry environment there are no changes in the mass or properties of the TPS materials. They are limited to relatively mild entry environments, for example, the Space Shuttle. The high temperature resistance of composites like carbon/carbon and carbon/silicon carbides enabled the development of reusable TPS. The amount of energy from the radiative and convective heating is re-radiated form the heated surface with the remainder conducted into the TPS material. High emissivity surfaces maximizes the amount of energy re-radiated and low surface catalycity to prevents the recombination of dissociated species, which can transfer additional heat to the surface [13]. It presents another advantage over the Ablative TPS if the primary isolation (inorganic) has low thermal conductivity because it will minimize the mass of material required to insulate the primary structure (backup material). One of the drawbacks of this type of TPS is the expensive maintenance requirement after each flight, including drying and replacement of the ceramic tiles and the restoration of the Silicon Carbides coating used as oxidation protection. Furthermore, the impacts with particles and birds is a big problem because of the fragility of these materials.

**Ablative TPS**. (Figure 2.1(b)). In contrast, these materials accommodate high heat loads by globally endothermic physico-chemical transformations and mass loss. Ablative TPS was used in the Apollo program because of the need for TPS able to withstand the return from lunar orbit. The ending of the shuttle program supposed the back to using ablative TPS and they can be seen again in the Orion and Commercial Crew Programme (CCP). These materials are reinforced composites employing organic resins as binders. When the heat increases, the resin pyrolyses producing gaseous products that permeate into the heated surface and are injected into the boundary layer. Carbonaceous residue produced by resin pyrolysis is deposed on the reinforcement as well. This resulting surface is called "char". The pyrolysis process is globally endothermic and the gases generated percolate towards the surface as well as transferring energy from the solid to the gas. It also generates a reduction in convective heating because

of the blockage effect. Moreover, this chemical reactions may have an effect in the consumption of the surface material leading to surface recession. The inconvenient with those kind of reaction is that they can be endothermic or exothermic and therefore have an important impact on the surface temperature. In comparison with the reusable TPS, theses ones are more complex as there are more mechanisms to manage the heating during the reentry.



(a) Reusable TPS structure　　　　　(b) Ablative TPS structure
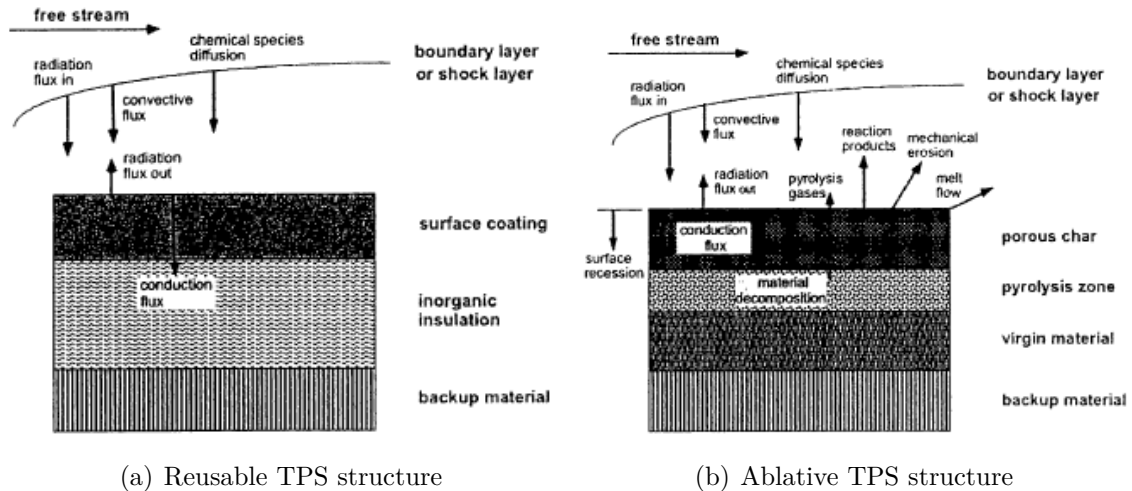
Figure 2.1: Energy accommodation of internal structure of the different types of TPS used on space heatshield. [13]

Experimental ablation studies are focused on the characterization of the Thermal Protection Materials (TPM) at certain conditions by means of ground-test facilities and numerical models. The data obtained is used to develop models about the material behaviour to predict the response during the whole mission. However, it is necessary to consider the huge amount of energy to reproduce the real conditions. To deal with this problem, at VKI there is a solution with affordable costs, this is, simulate hypersonic speed at low temperature in one facility and reproduce high temperature flux in a subsonic speed in other facility.

The hypersonic facilities are only allowed to reproduce the aerodynamic forces and compressible flow phenomena during several millisecond by a strong shock wave on the test model. However, the test times are not enough for having sufficient heat transfer to the surface in order to reproduce the chemical processes so it is necessary to use plasma-wind tunnels. These facilities use pure air at high enthalpies as a test gas so it is possible to simulate the aerothermochemistry of an atmospheric entry for several minutes through electric power. The main types of long duration plasma wind-tunnel are going to explain as follow.

**Induction Coupled Plasma (ICP)**. The one installed at VKI receives the name "Plasmatron". The plasma is generated by an induction-type plasma torch by means of electromagnetic induction. It is created by a high-frecuency induction coil surrounding a tube, often quartz, through which the test gas is injected. In this facility, the flow speed is usually subsonic which allows the gases to relax into thermochemical equilibrium and simplifies the boundary layer edge condition. The von Karman Institute Plasmatron facility is used in this project to reproduce the conditions of reentry plasmas in order to study the ablation process. [14].

**Arc-jets**. The gas is heated by an arc generated between anode and cathode in a converging-diverging nozzle. The flow is usually expanded to supersonic conditions at the outlet of the nozzle. However, the characterization of the flow is more difficult because of the erosion of the electrodes may pollute the flow.

The biggest difference lies in the way in which the plasma is generated, as well as the thermochemical state of the subsonic in Plasmatrons and supersonic in Arc-jets . Due to the high flow rates compared to the chemical relaxation times, the flux produced by the arc-jets is chemically frozen or none equilibrium state. In comparison with induction coupled plasma, higher heating rates are achieved and bigger sized models can be tested.

## 2.2 Photogrammetry concept

The three dimensional reconstruction of an object in digital form is the main purpose of a photogrammetric measurement. A two dimensional picture implies a loss of information from a three dimensional object, so for the reconstruction of an object from images, it is necessary to describe the optical process by which an image is created.

The technique used in this work is categorized within the field of photogrammetry and is called stereophotogrammetry. It consists of dual image processing and stereoscopic measurement, so from the intersection of two separated image rays, an object point can be located in three dimensions.

The pinhole camera model is the simplest one, so it will be explained to understand the physics of the cameras. All image rays pass through the centre $c$ and they form an image by projecting onto an image plane. The size of the image relative to the object depends on a single parameter of the camera, which is the focal length as can be seen in Equation (2.1). In the Figure 2.2, $f$ represents the focal length of the camera, $Z$ is the distance from the camera to the object, $X$ is the length of the object and $x$ is the length of the object projected on the imaging plane.

$$-x = f \cdot \frac{X}{Z} \tag{2.1}$$
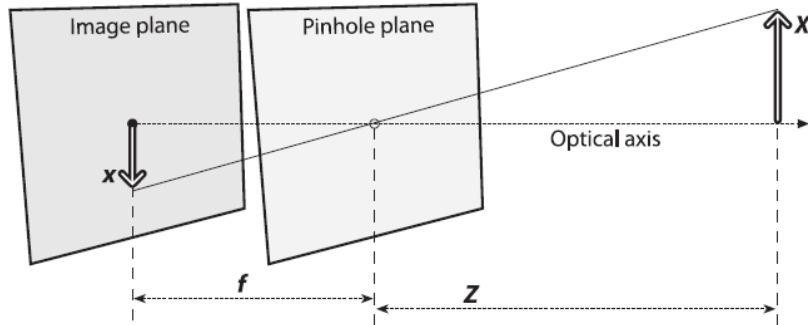


Figure 2.2: Pinhole camera model. The image is projected onto an image plane by the rays that intersect a particular point in space determined by the pinhole aperture. [9]

The center of the image chip is usually not on the optical axis because the manufacturing is not perfect, so two new parameters need to be introduced, $c_x$ and $c_y$. They model the possible displacement from the optic axis of the center of coordinates on the image plane and these coordinates are given by the Equation (2.2) and (2.3).

$$x_{screen} = f_x \cdot \frac{X}{Z} + c_x \tag{2.2}$$

$$y_{screen} = f_y \cdot \frac{Y}{Z} + c_y \tag{2.3}$$

Finally, the last parameter defined are the two different focal lengths because a camera might not have squared pixels. In order to take into account this effect, $f_x$ and $f_y$ will be defined as the product of the physical focal length F and the size $s_x$ and $s_y$ of the individual imager elements (Equations (2.4) and (2.5)). In addition, $s_x$ and $s_y$ can not be measured directly from camera calibration and the focal length either. Only the values $f_x$ and $f_y$ can be measured directly without dismantling the camera.

$$f_x = F \cdot s_x \tag{2.4}$$

$$f_y = F \cdot s_y \tag{2.5}$$

Although, it is possible to define theoretically a lens with no distortions, in practice it supposes a big deal because it much more easier to make a lens spherical instead of a mathematically ideal parabolic. Additionally, it is difficult to mechanically align the lens and image exactly. Radial distortion is the result of the shape lens whereas

Tangential distortion is related with the assembly process of the camera.

Firstly, the radial distortion is caused by the lenses because they distort the location of pixels near the edges of the image. Rays further from the center of the lens are bent more than those that are closer. In the Figure 2.3 can be seen this phenomena. This distortion can be characterized by the first few terms of a Taylor expansion, so for conventional cameras two such terms are used called $k_1$ and $k_2$. However for highly distored cameras such as fisheye lenses is commonly used a third term $k_3$. The radial location of the point of the imager can be rescaled according to the equations (2.6) and (2.7).
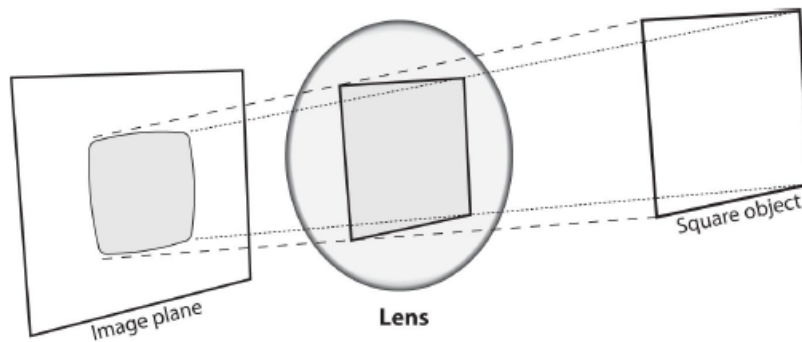


Figure 2.3: Radial distortion. Rays far from the center bent too much compared to rays that pass closer. [9].

$$x_{corrected} = x \cdot (1 + k_1 \cdot r^2 + k_2 \cdot r^4 + k_3 \cdot r^6) \tag{2.6}$$

$$y_{corrected} = y \cdot (1 + k_1 \cdot r^2 + k_2 \cdot r^4 + k_3 \cdot r^6) \tag{2.7}$$

Secondly, the tangential distortion is due to a manufacturing defect. The lens is not exactly parallel to the image plane as it can be seen in Figure 2.4. Tangential distortion is characterized by two more parameters p1 and p2 and the corresponding equations (2.8) and (2.9).

$$x_{corrected} = x + [2 \cdot p_1 \cdot x \cdot y + p_2 \cdot (r^2 + 2 \cdot x^2)] \tag{2.8}$$

$$y_{corrected} = y + [p_1 \cdot (r^2 + 2 \cdot y^2) + 2 \cdot p_2 \cdot x \cdot y] \tag{2.9}$$

To project the physical world coordinates $(X, Y, Z)$ to the points on the projection screen with coordinates $(x, y)$ is used a projective transformation. In such transform, it is useful to use homogeneous coordinates, so the projection of physical world points
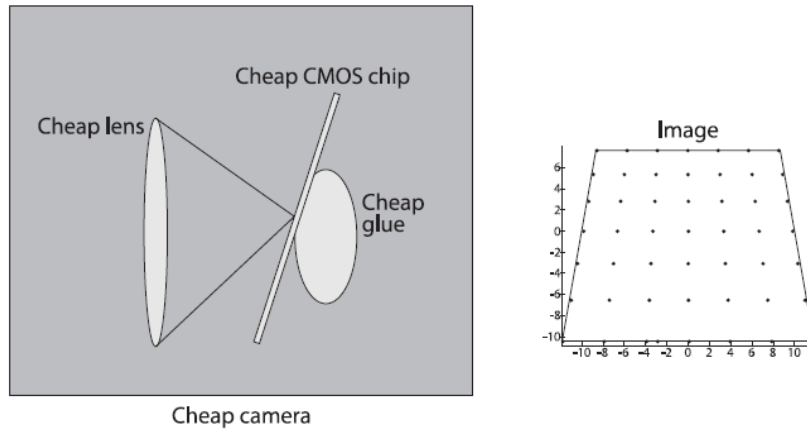
Figure 2.4: Tangential Distortion. It appears when the lens is not completely parallel to the image plane. [9].

into the camera is represented in the Equation (2.10).

$$\text{q} = \text{M} \cdot \text{Q}, \ \text{q} = \begin{bmatrix} x \\ y \\ w \end{bmatrix}, \ \text{M} = \begin{bmatrix} f_x & 0 & c_x \\ 0 & f_y & c_y \\ 0 & 0 & 1 \end{bmatrix}, \ \text{Q} = \begin{bmatrix} X \\ Y \\ Z \end{bmatrix} \tag{2.10}$$

Where q represents the homogeneous vector of camera coordinates, M is the camera intrinsic matrix, and Q is the homogeneous vector of physical world points in camera coordinates.

### 2.2.1 Stereo imaging

The stereo imaging is very similar to the stereo capability of the human eyes, so the main goal is to emulate this capability in computer systems. Computers are capable to find corresponding points between both images, so with such correspondences and a known baseline separation between cameras, it is possible to calculate the 3D location of the points. The search for corresponding point can be done automatically with a high computationally cost or knowing the geometry beforehand, it can be limited the search space as much as possible. There are four steps to follow when using two cameras in stereo imaging.

- Remove radial and tangential lens distortion mathematically in order to get undistorted images.

- Adjust angles and distances between cameras to get row-aligned and rectified images.

11

- Find the corresponding feature points in the right and left camera images in order to get the disparity map. It represents the differences in x-coordinates between left and righ cameras $(x_l - x_r)$.

- By knowing the geometrical arrangement of the cameras, the disparity map can be converted into distances by triangulation. Through this process called reprojection, the depth map is obtained.

### 2.2.2 Triangulation

Imagine a situation with two cameras whose image planes are exactly co-planar with each other, with exactly parallel optical axes and with equal focal lengths $f_l = f_r$, this is a perfectly undistorted, aligned and measured stereo rig as is shown in Figure 2.5. Additionally, assume that principal points $c_x^{left}$ and $c_x^{right}$ are calibrated to have the same pixel coordinates in their respective images. It is possible to find a point $P$ in the real world in the left and right image views $p_l$ and $p_r$ and their respective horizontal coordinates $x^l$ and $x^r$. Then, the disparity, that is defined by $d = x^l - x^r$ is inversely proportional to the depth, so the depth can easily derive by using similar triangles (Equation (2.11)).

$$\frac{T - (x^l - x^r)}{Z - f} = \frac{T}{Z} \rightarrow Z = \frac{f \cdot T}{x^l - x^r} \tag{2.11}$$

As the disparity is inversely proportional to the depth, there is a non linear relationship, so for disparity values close to 0, there are larger depth differences. When the disparity is large, small variations in this value do not change the depth appreciably (Figure 2.6).

Figure 2.7 shows the 2D and 3D coordinate system for stereo vision. The image origin is located in the upper left part of the image and pixels are denoted by coordinates $(x_l, y_l)$ and $(x_r, y_r)$ respectively. After mathematical rectification the cameras are co-planar and horizontally aligned with the same focal length and separated a distance $T$.

Although it is relatively easy to solve for the distance with this arrangement, in a real camera setup, it is impossible to have the cameras exactly aligned in the frontal parallel configuration. Instead, image projections and distortion maps can be found using mathematical transformations. This allow the rectification into a frontal parallel arrangement. When designing the stereo rig, it is important to place the cameras as aligned with each other and with the sample as possible in order to make the mathematical transformations more tractable. Additionally, having synchronised cameras allows reconstruction of the objects moving or changing in the scene.
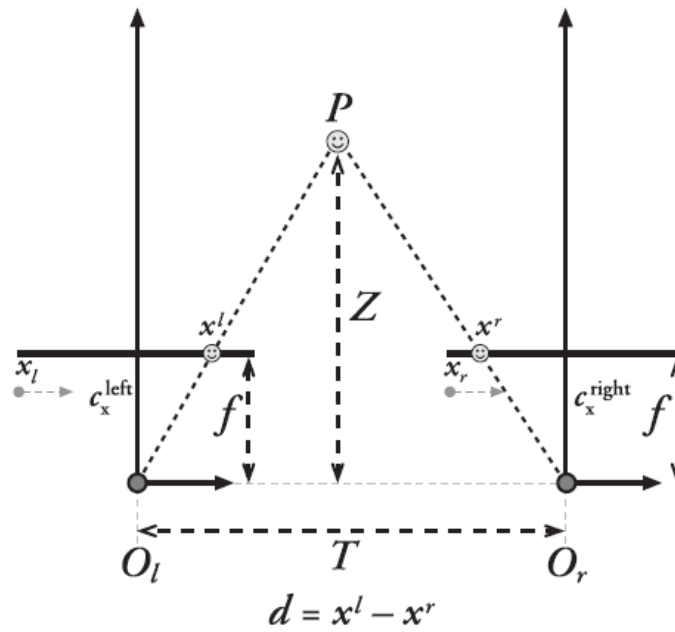
Figure 2.5: Scheme of the camera arrangement needed to calculate the depth $Z$ by similar triangles. [9]
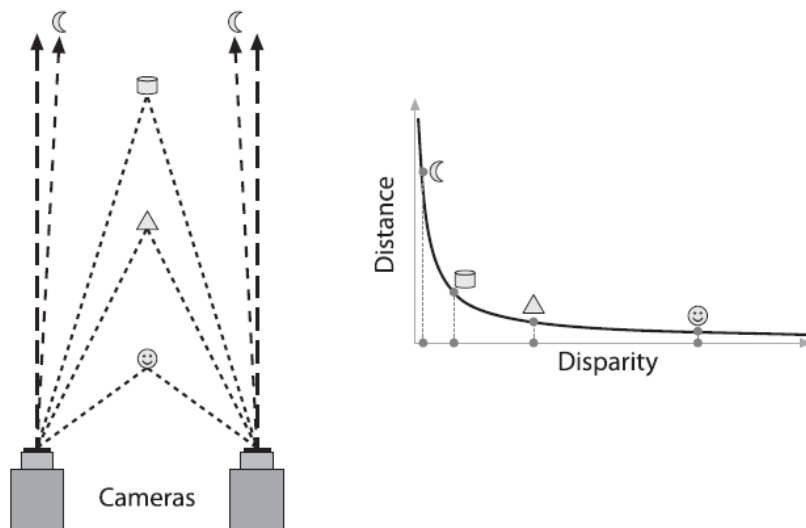


Figure 2.6: Distance vs disparity. These parameters are inversely proportional because the smaller the distance, the bigger the angle and the points in common between pictures are less . [9]
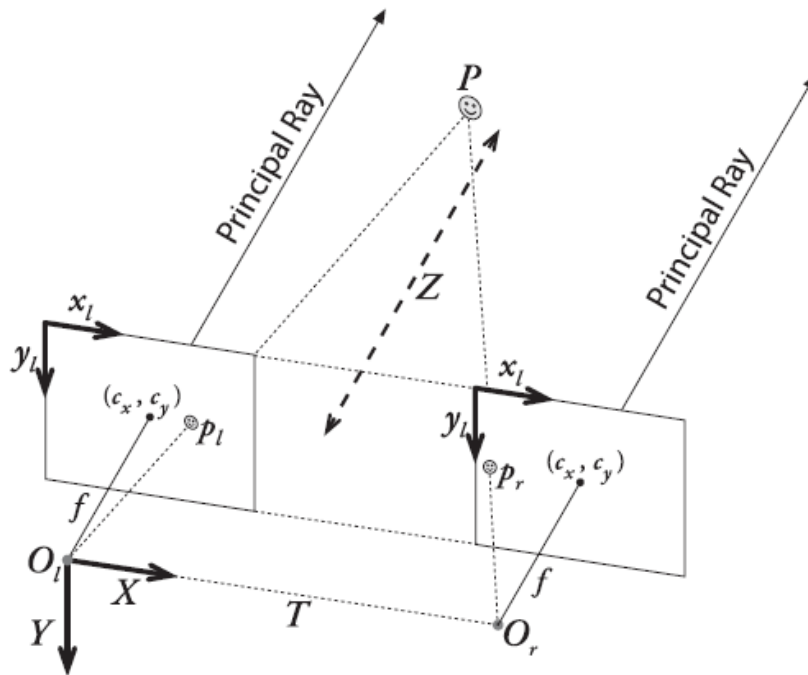
Figure 2.7: Stereo coordinate systems used by Open CV to calculate the coordinate of point P in 3D for undistored rectified cameras. [9]

### 2.2.3 Epipolar geometry

Epipolar geometry represent the base of the geometry of a stereo imaging system (Figure 2.8). This geometry combines two pinhole camera models and new points called the epipoles. For each camera there is a center of projection $O_l$ and $O_r$ and two corresponding projective planes $\Pi_l$ and $\Pi_r$. The projections of a real point $P$ in these projective planes are labelled as $p_l$ and $p_r$. The new points are the epipoles $e_l$ and $e_r$ located on the image plane $\Pi_l$ and $\Pi_r$. They are defined as the projection of the center of projection of the other camera $O_r$ (respect $O_l$). The plane is formed by the real point P and the two epipoles $e_l$ and $e_r$.

When a point in the physical world is projected onto the right or left image plane, this point can be located anywhere along the entire line of the ray going from $O$ through $p$ because with one camera can not be known the distance to the point. In other words, the image of all the possible locations of a point $P$ seen in one imager is the line that crosses the corresponding point and the epipolar point in the other image camera.

Finally, all the facts about stereo camera epipolar geometry are summarized as follows:

- Every 3D point in the view of both cameras is contained in an epipolar plane
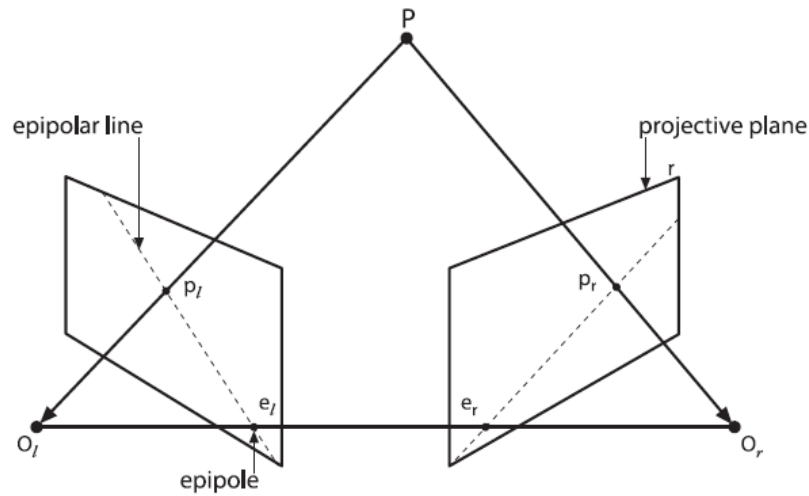
Figure 2.8: Epipolar geometry. The plane is defined by the observer point P and the two center of projections. [9]

- Epipolar constraint gives a characteristic in an image. The coincident view must be along the epipolar line of the other image

- Once the epipolar geometry stereo rig is known, the 2D search for matching feature points across two imagers, becomes a 1D search along the epipolar line.

- If the points A and B that are visible in both images appear horizontally in that order in one of the images is also appear in the other image.

## 2.2.4   The Essential and Fundamental Matrices

These matrices contain information about the rotation and translation between two cameras (matrix E) in the space as well as the information about the intrinsic of both cameras (matrix F).

The matrix E contain the information about the location in physical coordinates of the point P seen by the left camera to the location of the same point as seen by the right camera. Instead, the fundamental matrix F represents the points on the image plane in image coordinates in pixels to the points on the image plane of the other camera in image coordinates.
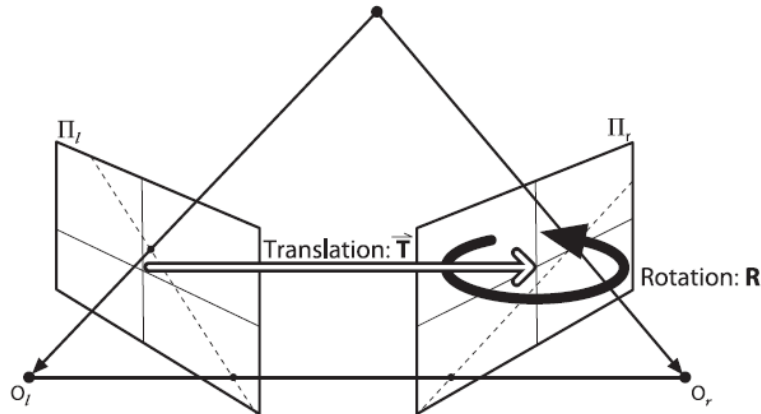
Figure 2.9: Rotation and Translation scheme. Matrix E contains the information about the essential geometry of stereo imaging, which contains the information about translation T and rotation R. [9].

## 2.3 Camera Parameters and Configuration. Photography

This section is very related with the experimental part of the project. Photography concept and the camera parameters are useful for the reader to know how to configure the cameras taking into account the luminosity conditions during each experiment. It is important in order to take pictures with good quality, avoiding over and under exposure areas, blurry parts of the sample, etc.

### 2.3.1 Sensor

Sensors convert light into electric charge and process it into electronic signals. There are two types of sensors: Charge Coupled Device (CCD) and Complementary Metal Oxide Semiconductor (CMOS). In a CCD sensor every charge of a pixel is transferred through a very low number of output nodes, normally just one, to be converted to voltage, stored and sent outside the chip as an analog signal. The output's uniformity and the high quality image are due to every pixel can be dedicated to light capture. In a CMOS sensor, the charge-to-voltage conversion is done by each pixel and usually, the sensor includes noise correction, amplifiers and digitization circuits for the chip to produce digital bits. These functions reduce the area available for the light capture because of the design complexity. Additionally, the uniformity is lower because each pixel does its own conversion but it allows higher total bandwidth for high speed.[15]

The most important parameters for machine vision are the speed and noise. As explained before, the difference between both types of sensors is the way signals are converted from signal charge to an analog signal and finally to a digital signal. In

16

CMOS area the front end of this data path is parallel allowing each amplifier to have low bandwidth. In contrast, high speed CCD has higher bandwidth, which results in higher noise. Definitely, high speed CMOS imagers can be designed to have much lower noise than high speed CCD.
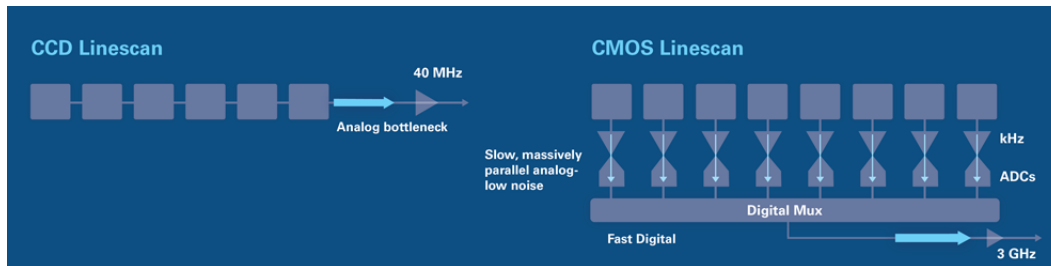


Figure 2.10: Internal structure of CCD vs CMOS sensor. [15]

Finally, two important characteristics to take into account to choose the type of sensor are the blooming and smear performance. These concepts consist of the interference between the charge collected by a pixel on adjacent pixels. They can reduce the pixel data information because the total information from one pixel is shared in adjacent pixels. The problem occurs when there are very bright points in the scene. CMOS presents a big advantage and has better control in these phenomena, so this is the type of sensor of the cameras because during the experiments in the VKI Plasmatron whose brightness condition are very high. [16]

### 2.3.2 Camera Exposure

Exposure is the amount of light that enter in the camera sensor. It can be controlled by the exposure time (or shutter speed), the F-number (or aperture) and the Gain (or ISO speed), so these parameters make up the "Exposure Triangle". It is necessary to reach the correct combination of these parameters in order to take a picture with high quality avoiding the loss of information in some pixels. Depending on the application and the light conditions during the experiments the values of these parameters may change.

**Shutter Speed (Exposure Time)**

Shutter speed is the amount of time that the sensor is receiving light from the scene. The longer the shutter is open the more light is allow to hit the sensor. Exposure time is the inverse concept. Apart from control the amount of light captured by the sensor, this parameter can affect in a picture taken of a motion scene. High values of exposure time will blur motion, while low values can freeze action.
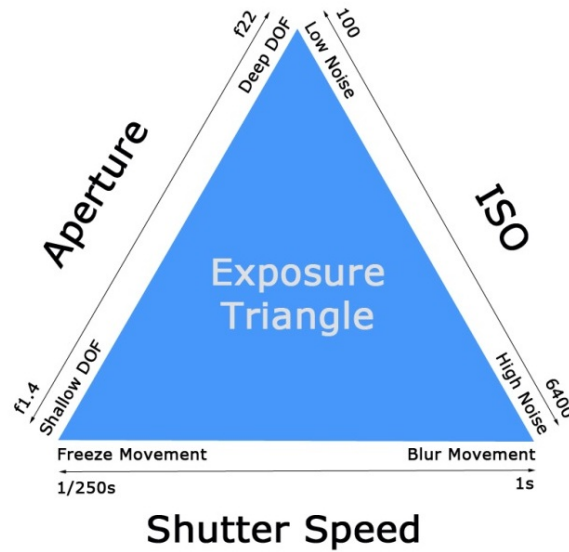
Figure 2.11: Exposure Triangle. Parameters that can be controlled directly by the camera and the secondary effects of each parameter. [17]

For this application, due to the very brightness conditions during the VKI Plasmatron experiments, the exposure time needs to be as lower as possible to reduce the amount of light in the sensor to avoid over-saturated parts (common value between $50\,\mu$s and $500\,\mu$s). This is also a positive aspect because the area of the sample where the material is degrading and can introduce movements in the scene will be freeze.

In the experiments outside the VKI Plasmatron, the scene is completely static and the light conditions are lower, as the cameras are mounted on a tripod to avoid the camera shake there is no problem to increase the exposure time to higher values ($8 \cdot 10^5 \mu s$).

**Aperture (F-number)**

The aperture is the size of the opening in the lens. The lens is the first element of the camera where the light goes through and it controls the maximum amount of light that can hit the sensor. A bigger aperture lets more light in and vice versa. F-number is a parameter to determine how open or close is the lens depending on the aperture diameter. This emphasizes the relationship between the aperture and the focal length. The lower the value of the F-number, the bigger the aperture hole and more light reaches the sensor.

The aperture has a secondary effect on the depth of field:

- Large apertures, that means low F-number tend not to focus the background of the images

- Small apertures, that means high F-number tend to have more part of the scene in focus.

In this project, as said before, the amount of light emitted by the VKI Plasmatron during the experiments is very high so the aperture is configured in the lowest position which is the high F-number in order to reduce the light that hit sensor. This is a positive aspect because the depth of field will increase and also the sharpness in the image to have a good information in every pixel of the picture.

**ISO (Gain)**

The ISO is the sensitivity of the sensor to the light that is hitting it. The higher the number, the more sensitive is the sensor and more light will be captured. There is another parameter which causes the a similar effect that is the Gain. It is defined as an electronic amplification of the video signal, adding more voltage to the pixels causing them to amplify their intensity and therefore brighten the image. A secondary effect is that increasing gain or ISO increase image noise or grain.

### 2.3.3 Focal length

The focal length of a lens is the distance between the optical center of the lens (where the lens is located) and the sensor (or focal plane, where the image is generated). Through the focal length, the field of view and the size of the object in the image can be determined. The lower the focal length, the higher the field of vision, and the higher the part of the scene included in the photograph. On the contrary, the higher the focal length, the smaller the field of vision, and the smaller the area of the captured scene.

In this project, the lenses used have a fixed focal length to make sure that both cameras have the same value and to avoid changes during the configuration. To have the field of vision or the size of the sample in the experiments, it is necessary to change the distance from the cameras to the sample.

The optimum case is to use a lens with a focal length to have the maximum part of the frame as possible occupied by the sample in order to have information in the maximum number of pixels as possible. The parameter defined Region of Interest (ROI) can be used when this configuration is not possible, it means, the resolution of the picture can be reduced to have information in the maximum part of the frame as possible.
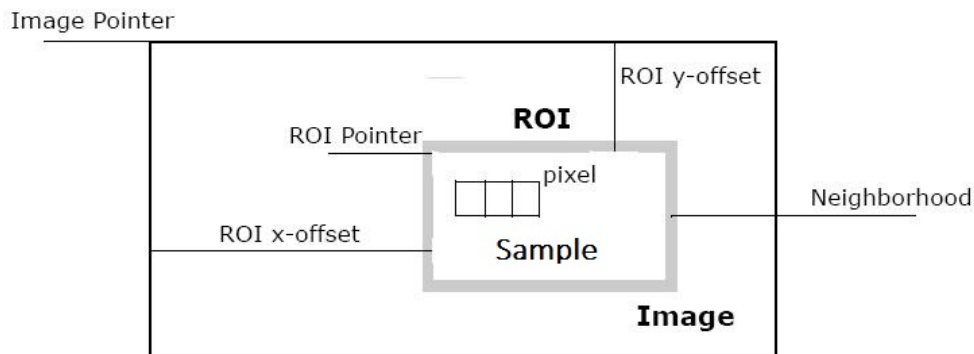
Figure 2.12: Region of Interest. Part of the complete resolution of the camera that appears in the picture. [18]

## 2.3.4 Brightness Histogram

The brightness histogram is a statistical graph of the tones (or brightness levels) of the scene captured by the camera. This tool gives information about the exposition of the picture. The user can determine if the picture is overexposed (when the histogram is skews to the right edge of the graph) or underexposed (when the histogram skews to the left edge of the graph) some parts of the scene. Figure 2.13 represents the three cases with different exposure. In many cases is preferable to have under-exposure parts in the pictures than over-exposure to avoid the loss of information in those pixels.

(a) under-saturated picture

(b) under-saturated histogram



(c) good picture

(d) histogram



(e) over-saturated picture

(f) over-saturated histogram
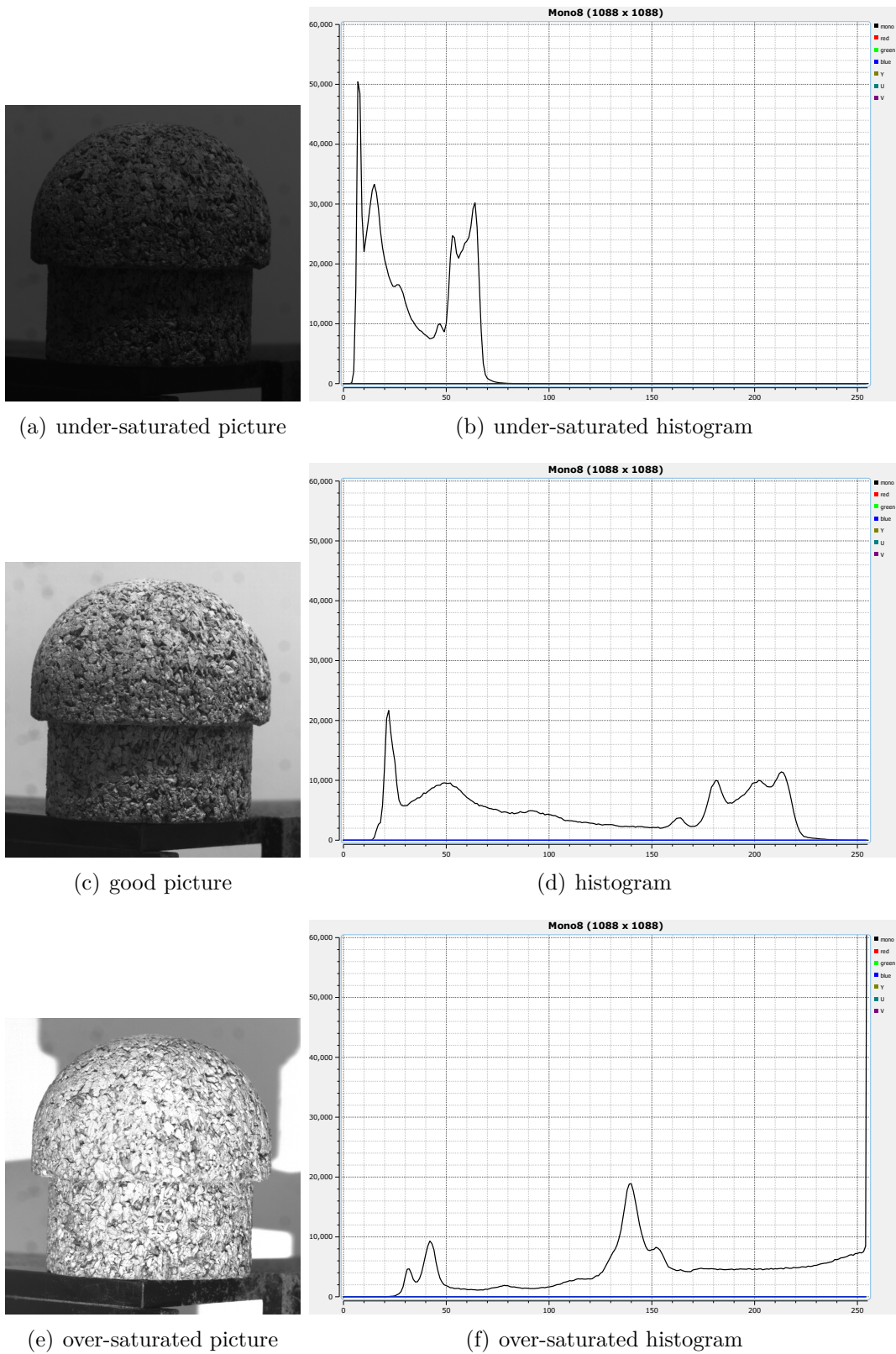
Figure 2.13: Pictures of the sample with different luminosity and their corresponding histogram. In under-saturated pictures there are more pixels with black tones (left part of the plot) while in over-saturated pictures there are more pixels with white tones (right part of the plot).

### 2.3.5 Neutral Density Filter

The neutral density filter (NDF) reduces of modifies the intensity of all wavelengths. It is a piece of glass or semi-transparent resin that is placed in front of the lens. The filter allows to reduce the light that reaches the sensor avoiding overexposing the scene [19]. There are two types depending on the way that it reduces the light (Figure 2.14):

- Neutral density filters (ND) that limit the light evenly across its surface.

- Graduated neutral density (GND) filters that gradually limit light (not uniformly) along its surface. These types of filters are very useful for photographing high contrast scenes, it means, when one region of the image is bright and the rest is not.



(a) Uniformed Neutral Density Filter    (b) Graduated neutral density filter
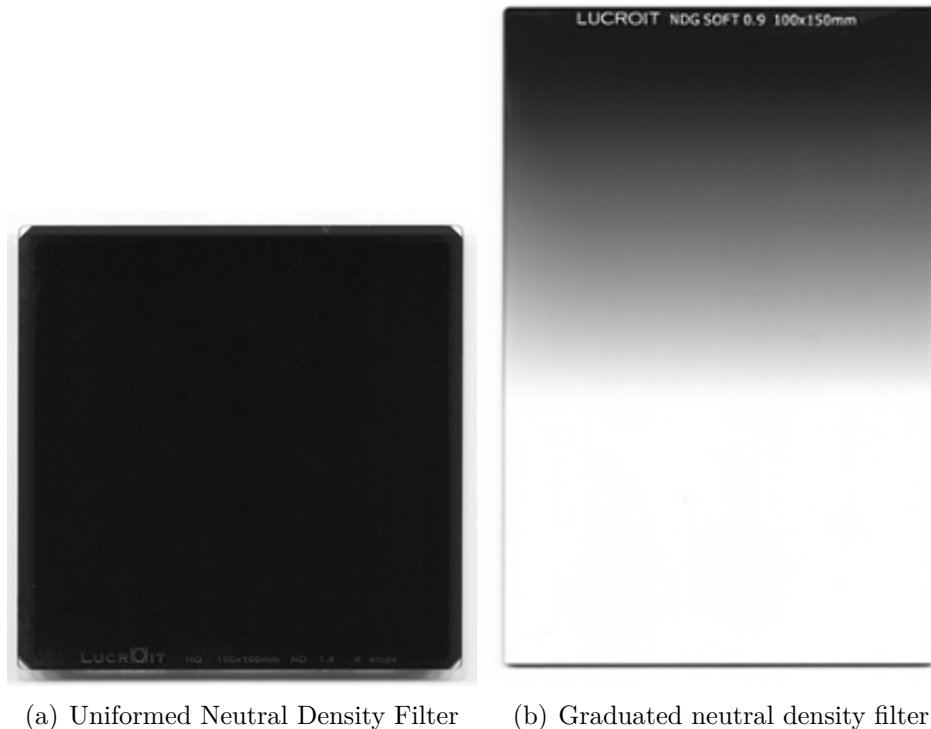
Figure 2.14: Type of filters proposed to use in cameras to avoid over-saturated parts in pictures during the VKI Plasmatron experiments. [19]

For this application, a GND filter is more adequate because the whole sample is not at the same brightness conditions. the front part of the sample, where the plasma hit, is the most brightness part and, then there is a smooth transition until the end. In the Section 4 can be seen this phenomena. Because of the lack of time, it was not possible the implementation during the experiments.

## 2.4 Optimization Method for the Reconstruction Code by Dakota

Once, the three main topics have been explained, there is another theoretical topic related with the optimization of the most influencing input parameters of the reconstruction code to get the best reconstruction possible. The optimization algorithm consist of the minimization of the Mean Squared Error (MSE) between a known geometry (introduced through a mathematical function or a CAD design) and the cloud points given by the reconstruction code.

The tool used to manage this optimization is DAKOTA 6.7 which is the state-of-the-art research and robust, usable software for optimization. The structure of optimization algorithm is represented in Figure 2.15)
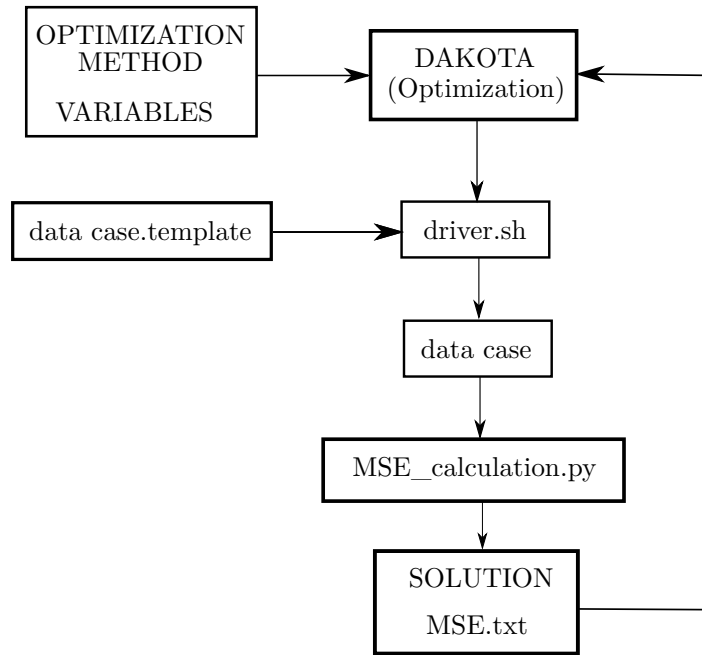
Figure 2.15: General structure of the dakota algorithm. The inputs parameters, which are the optimization method and the variables can be defined by the user. The solution for this application is the minimum MSE.

The Equation (2.12) represents the MSE between the number of points ($np$) calculated by the reconstruction code (*simul*) and the points calculated from the mathematical expression which defines the geometry of the sample (*calib*).

$$MSE = \frac{1}{np} \sum_{i=0}^{np} \left| P_{(x,y,z)}^{simul} - P_{(x,y,z)}^{calib} \right|^2 \tag{2.12}$$

23

A sensitivity analysis has been done in a parallel project [20] to study influence of the input parameters in the 3D reconstruction through the MSE. This is useful to reduce the number of inputs in the optimization process and hence the computational cost.

Figure 2.16 shows the optimization methods implemented in DAKOTA. To select an optimization method, a multitude of factors must be taken into account. For example the improvement goal and the (single or multi) objective. Also the bounds for each variable, linear and non-linear constraints, as well as, discrete or continuous variables. Global or Local optimization depending on the application and the number of optimum solutions. Finally, determine what are the problem characteristics, including cost and robustness.

| Category | Dakota method names | Continuous Variables | Categorical/ Discrete Variables | Bound Constraints | General Constraints |
|---|---|---|---|---|---|
| **Gradient-Based Local (smooth)** | `optpp_cg` | x | | | |
| | `dot_bfgs, dot_frcg, conmin_frcg` | x | | x | |
| | `npsol_sqp, nlpql_sqp, dot_mmfd, dot_slp, dot_sqp, conmin_mfd, optpp_newton, optpp_q_newton, optpp_fd_newton` | x | | x | x |
| **Gradient-Based Global (smooth)** | `hybrid, multi_start` | x | | x | x |
| **Derivative-Free Local (nonsmooth)** | `optpp_pds` | x | | x | |
| | `coliny_cobyla, coliny_pattern_search, coliny_solis_wets, surrogate_based_local` | x | | x | x |
| | `asynch_pattern_search, mesh_adaptive_search` | x | x | x | x |
| **Derivative-Free Global (nonsmooth)** | `ncsu_direct, genie_direct, genie_opt_darts` | x | | x | |
| | `coliny_direct, efficient_global, surrogate_based_global` | x | | x | x |
| | `coliny_ea, soga, moga (multiobjective)` | x | x | x | x |

Figure 2.16: Optimization methods implemented in DAKOTA grouped according to their characteristics. [21]

The methods used in this project are the followings. They are selected in order to try one method of each group in order to study which characteristics are most adequate for the application with the reconstruction code.

- **conmin_frcg**: is a conjugate gradient optimization method. The advantage to use this method is that reconstruction code is a smooth function. Additionally, this methods is used to find local optimum. The initial point is given by the sensitivity analysis so it is very close to the optimum solution. One inconvenient of this method is that only one point can be calculated at the same time because the solution in each iteration will be needed to calculate the next step.

- **asynch_pattern_search**: consists of a technique based on an asynchronous pattern in which the search along each offset continues without waiting for searches along other direction to finish. This method converges to a local extreme.

- **soga**: is a genetic algorithm. It is a global optimization and can support general constraints and a mixture of continuous and discrete variables. This algorithm does not take account the initial values obtained by the sensitivity analysis but through the lower and upper bounds, the region of interest will be reduced, increasing the convergence velocity.

# Chapter 3

# Materials and Methods

In this chapter, all the experimental tools used during this project to carry out the experiments and the measurements of the ablation process will be presented. First of all, the VKI Plasmatron facility which reproduces the plasma flow field and where the experiments take place, the current technique based on the high speed camera used to characterize the ablation process and finally the measuring devices used for the stereo photogrammetry technique that is the main aim of this project.

## 3.1 VKI Plasmatron facility

The VKI Plasmatron facility reproduces the aerothermodynamic environment of reentry plasma flows through a high-enthalpy, highly dissociated subsonic gas flow. The full scheme of the VKI Plasmatron system is shown in Figure 3.1.

The ICP torch injects the ring-shaped gas into a cold cage of 160 mm internal diameter. This is placed inside a quartz tube of 200 mm internal diameter and surrounded by a single-turn flat coil inductor. This coil is powered by a high frequency generator of MOS technology (400 kHz, 1.2 MW). With a 1.7 MVA transformer and a 12 pulses bridge with smoothing choques, the 11 kV, 50 Hz voltage from the electrical grid is adapted and rectified [1].

The initial ignition of the torch is performed with Argon (Ar) because its ionization energy is lower than the air molecules, that first have to be dissociated. Strong electric field currents create an initial spark which introduces electron into the argon gas stream. Then, the electro-magnetic field accelerates them to allow the collision with argon atoms and further ionization. The creation of new electron through collisions and also the recombination of electron with argon ions make it a well-balanced process. The next step is to switch to the desired test gas, for example, air, $CO_2$ or $N_2$. The process can run uninterruptedly provided enough electricity, supply gas and cooling once the
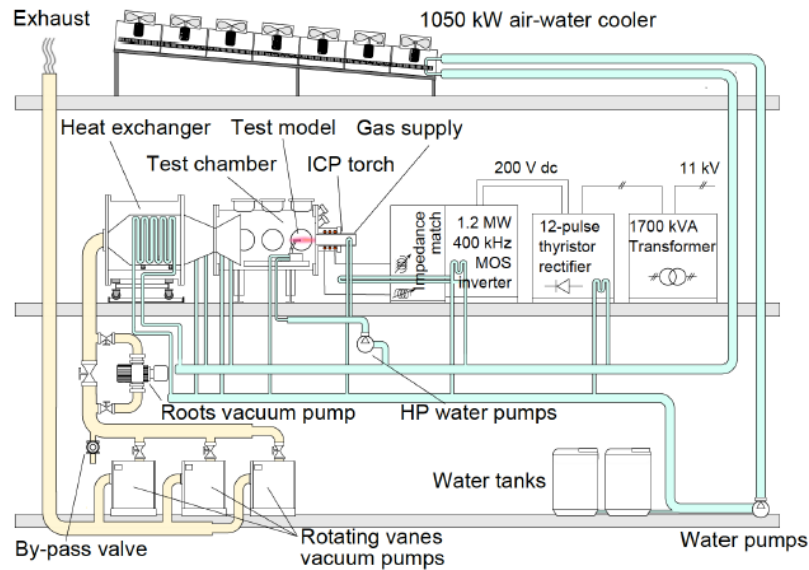
Figure 3.1: Schematic of the VKI Plasmatron system. [1].

equilibrium is reached.

The torch, test chamber, sample retention system, and holding arms are refrigerated by a 1050 kW cooling system which supplies a closed water loop (2090 l/min) and a fan-driven air coolers on the roof. The vacuum system consists of a three rotary-vane pumps and a roots pump. They are capable of extracting $3900\,\mathrm{m^3/h}$ and of vacuum the test chamber to a pressure of $2\,\mathrm{Pa}$.

In the Figure 3.2 can be seen the visual accesses of the VKI Plasmatron where the cameras can be placed. There are 6 windows in total but it necessary to take into account the other measuring devices in order to planning the camera arrangement. As stated in previous sections, two cameras are required for the stereo photogrammetry technique, so different configurations will be tested in order to get the optimal one for the reconstruction code.

(a) front side

(b) right side
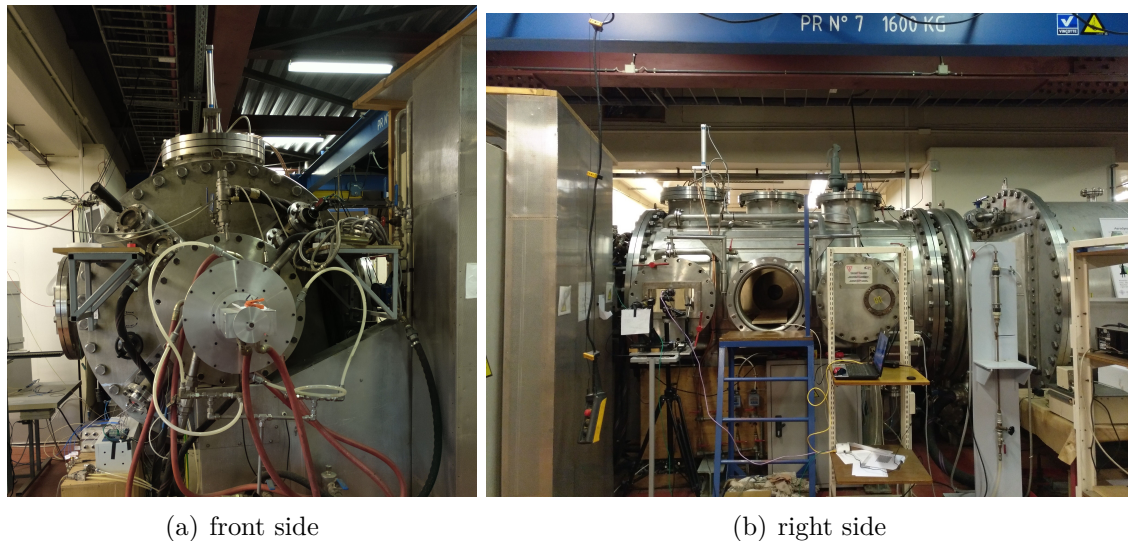
Figure 3.2: Views of the VKI Plasmatron facility

## 3.2 Cameras

In this section, the cameras used on the experiments are presented on the Figure 3.3 and 3.4. They were provided by two different manufacturers which are Allied Vision and Stemmer Imaging. There are 4 cameras in total and it is important to note that there are two different models of the Prosilica GT cameras. Although, one of the requirements to apply the stereo photogrammetry reconstruction code is that the cameras must be the same, these cameras are provided by the same manufacturer (Allied Vision) and the models are quite similar so they can be configured through the software in order to have the same resolution, frame rate, exposure time, etc.

Comparing the specifications of each camera, the ones provided by JAI manufacturer present better characteristics because the resolution, the frame rate or the efficiency are higher than the Prosilica GT cameras. Moreover, Prosilica GT cameras are C-mount while the lenses are F-mount, so an adapter is needed to mount the lenses to the cameras as is shown in the Figure 3.7. The type of sensor in all of them is CMOS which have better control of blooming and this is positive in order to take pictures in the brightness conditions during the experiment on the VKI Plasmatron.

The characteristics of each camera are presented in the Table 3.1.

This project is not only the first time that the cameras have been using during the Ablation tests in the VKI Plasmatron but also the first time that have been triggered to take pictures synchronously so it has been necessary to figure it out.

On the one hand, for the Prosilica GT, there are two ways of triggering: trigger

(a) GT2000             (b) GT2000

(c) GT2050 back        (d) GT2050 back

Figure 3.3: Prosilica GT cameras used during the experiment



(a) Front             (b) Back

Figure 3.4: SP-12000 CXP-4 cameras used during the experiment

| Camera | GT 2000 | GT 2050 | SP-12000-CXP4 |
|---|---|---|---|
| Resolution (MP) | 2.2 | 4.2 | 12 |
| | 2048 (H) x 1088 (V) | 2048 (H) x 2048 (V) | 4096 (H) x 3072(V) |
| Sensor | CMOSIS/ams | CMOSIS/ams | APS-C CMOS |
| | CMV2000 | CMV4000 | |
| Frame rate (fps) | 53.7 | 28.6 | 189 |
| Efficiency (%) | 75 | 79 | 99 |
| Full frame | No | No | Yes |
| Connection | Ethernet | Ethernet | CoaXPress |
| Lens mount | C-mount | C-mount | F-mount |

Tabla 3.1: Main characteristics of the cameras.

over Ethernet and external trigger using the 12 pin port. The first one consists of triggering the cameras through the software Vimba Viewer (software provided by the manufacturer of the cameras). The advantage of this method is the simplicity because it is only necessary 3 Ethernet cables Cat 6 and 1 switch as is shown in the Figure 3.5. The disadvantage of this configuration is that the cameras are not synchronized with the other measuring devices during the experiment. The other method using the 12 pin connector has not been implemented in this project but the cable configuration has been designed and is shown in the Appendix A.2. It will allow to synchronize with the other measuring devices used during the experiments to start the process of recording pictures.

On the other hand, for the JAI cameras, a software to triggering them had been developed previously this project [10]. However, the system need to be fixed because during one of the experiments a triggering problem with one of the cameras happened. Therefore, for the majority of the experiments the Prosilica GT cameras were used.

Figure 3.5: Switch to connect both cameras at the same computer to synchronize them.

In order to capture the majority of the sample into the frame of the picture the focal length of the lenses and the distance from the camera to the sample are the two most important parameters. As discussed above, the greater the focal length, the lower the field of view, so only the sample would be appear in the picture. In the VKI Plasmatron the distance from all the windows to the sample is around 1 m, so the focal length used is 50 mm as is shown in the Figure 3.6. In some cases another focal length of 105 mm was used.



(a) lens 50 mm                    (b) lens 50 mm

Figure 3.6: Lenses with focal length of 50 mm

|              (a) C-mount              |              (b) C-mount              |
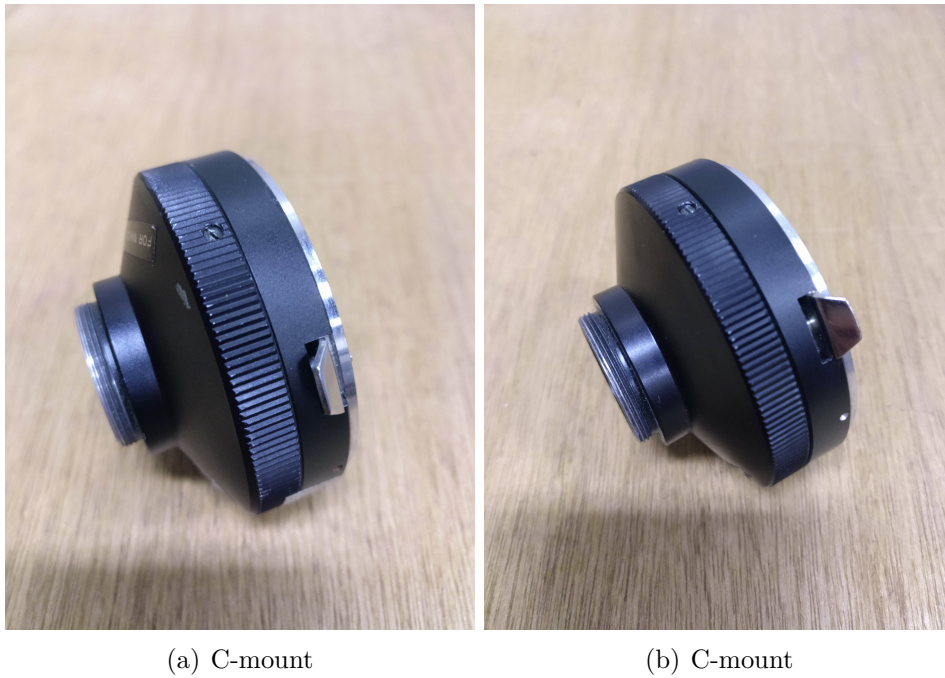
Figure 3.7: C-mount to attach the lenses to the Prosilica GT cameras

Finally, the cameras must be in the same position during the tests so it is necessary to place them in a tripod in order to avoid some movement. Additionally, the optics measuring devices has an special dimensions to attach them to the tripod, so it is necessary an special m5 screw as can be seen in the Figure 3.8.

(a) camera hole                    (b) screw
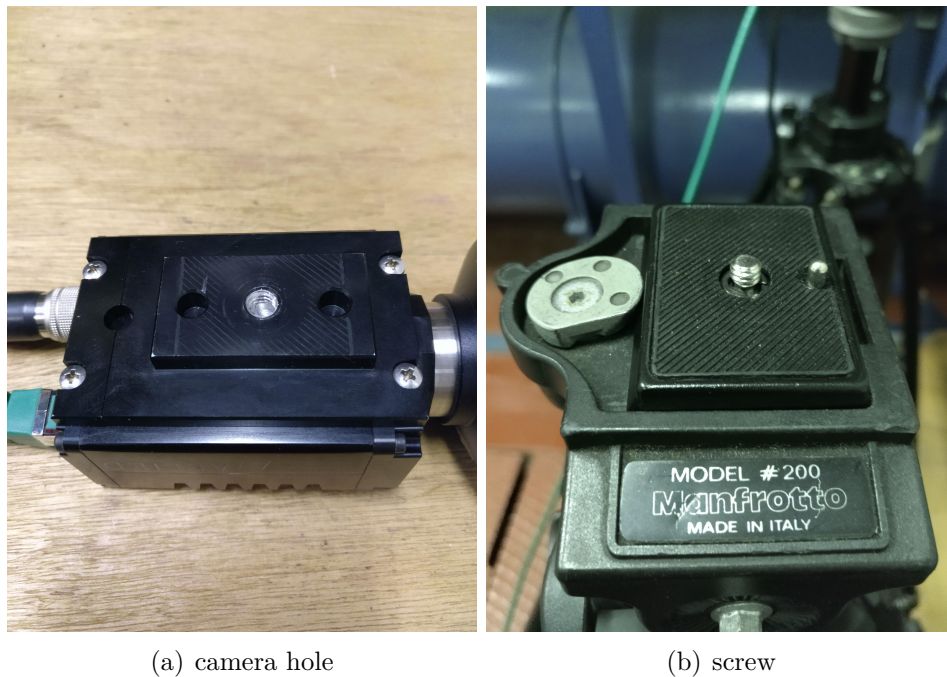
Figure 3.8: Screw m5 to attach the cameras to the tripod

## 3.3  Materials

There are several samples studied and each one was made of different material. In this section, the materials and their main properties and characteristics will be explained. Some of them were used only in test outside of the VKI Plasmatron while others were used during the test inside the VKI Plasmatron because they were real material used for space heat shields.

### 3.3.1  P45 and P50 Cork

Cork is the bark of the Cork Oak tree. The main property of cork is the insulation and has been used as a TPS from the beginning of space flight. Cork cells are small irregular pentagonal and hexagonal prisms and highly porous (50 % of volume is gas enclosed in cells), consequently it has low conductivity and low radiation between cells [22].

In this project, two types of cork composites have been used. P45 and P50 material consists of a cork composition made with cork granule and phenolic binders for high heat resistance [23]. Figure 3.9 shows the differences in the size of the granules. These materials are used as sheets of cork with specific thicknesses depending on the application. It is also used in areas that are hard to spray and is easy to cut and machine.

P45 was used outside of the VKI Plasmatron to develop the calibration of the cameras because the surface has more features easily to recognize by the software. P50 was used in the first test inside the VKI Plasmatron explained in Section 4.1 in order to configure the cameras.
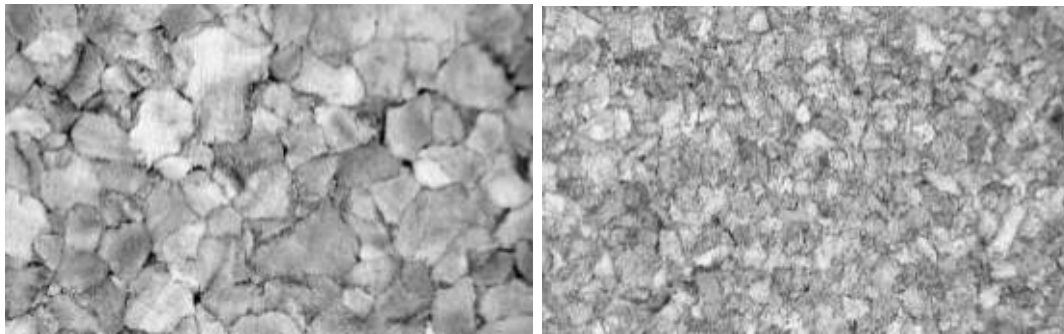


(a) P45 cork                                    (b) P50 cork

Figure 3.9: Surface of the different type of cork materials used in this project. a) and b) magnification: 50x. [23]

### 3.3.2   Graphite

Graphite is another material tested in this project inside the VKI Plasmatron because it can be considered as a simplified version of other materials (only carbon and there is no pyrolysis). It is also used as a TPS for spacecrafts. In the last years, a need has arisen to develop more resistant thermal protection systems capable of withstanding more aggressive reentry at higher speed [24].

This material will be used in future reusable TPS design owing to unique high temperature properties. In the absence of oxygen, this material can reach temperatures about 1600 °C without melting or softening and have high thermal shock resistance dimensional stability.

Graphite materials have high emissivity, low coefficient of thermal expansion (CTE) and are self-supporting at low and high temperature regimes. These characteristics permit utilization of both thermal insulating and conducting properties, respectively, within a thermal management system.

### 3.3.3   ZURAM®

ZURAM® is the last material tested inside the VKI Plasmatron and it is showed in Section 4.3. The ablative material ZURAM® is manufactured from a rigid carbon

felt impregnated with phenolic resin. It has a low density of approximately $0.36 - 0.4$ g/cm$^3$. The shape and dimensions are exactly the same as the P50 cork sample [25]. It is manufactured by DLR and is only used for researching studies.

## 3.4    Vimba Viewer

Vimba Viewer is the official software used to control the Prosillica GT cameras used for taking pictures in this project. This software allows to trigger and synchronize both cameras in order to take pictures each defined frequency. Also, through this software, the camera settings can be configured like the exposure time, the ROI, the frame rate, etc. The Installation Manual [26] explains all the information needed to use the cameras.

## 3.5    3D Reconstruction code

The development of a reconstruction code in an open source using the Python library Open CV has been done in a parallel project. This library has the tools to perform the 3D reconstruction with an uncalibrated stereo camera. The 3D reconstruction code was developed by Martinez G. [10] and improved by Cantos S. [20]. The application of this code is very reduced to this application because currently it only allows the reconstruction of a typical VKI Plasmatron sample.

This software uses two pictures of the sample taken by two cameras and 10 parameters as input to manage the 3D reconstruction. A sensitivity analysis has been done [20] in order to study the influence of the inputs parameters in the reconstruction solution. After that, these parameters are the focal length, the number of disparity and the minimum disparity.

Once, the most influencing parameters are defined, the next step is to find the best combination of these three input parameters that minimizes the MSE. For that, an optimization algorithm has been developed based on Dakota Software (Section 2.4).

Figure 3.10 illustrates the process followed by the code.

First of all, the feature matching consists of the recognition of the features in an object in one pair of stereo images. Instead of a calibration pattern, a highly structured image is used and the object should have as many features as possible in order to make easy the recognition and to avoid confusion during matching. The algorithm used by OpenCV is SIFT (Scale-Invariant Feature Transformation).
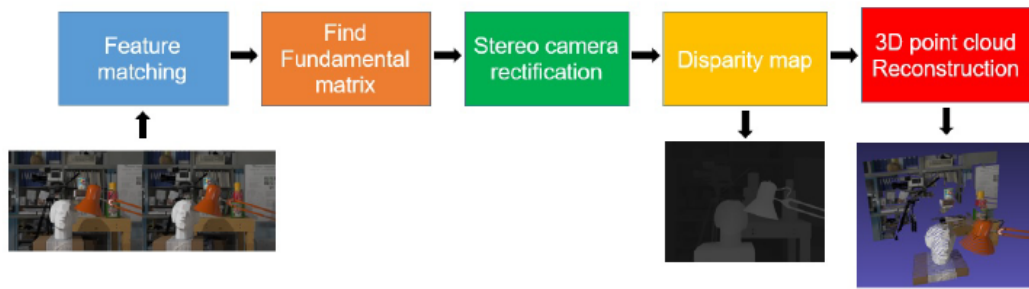
Figure 3.10: Scheme of stero 3D Reconstruction with uncalibrated method. [10].

Once the positions of feature points are calculated and stored as image points, the algorithm RANSAC (Random Sample Consensus) calculates the fundamental Matrix F. The next step is the stereo camera rectification. The result is the rectification transformation without knowing the intrinsic parameters of the cameras and its relative positions. Then, the disparity map of the rectified image pair needs to be found. It can give information about the depth of a certain point. In order to obtain a disparity value, the point must be found in both images, otherwise this point can not be reconstructed.

Finally, the 3D point cloud reconstruction is made by the disparity-to-depth mapping matrix Q, proportioned manually. It is assumed that the principal point is in the center of the image, so $c_x$ and $c_y$ are the half of the width and height respectively. Knowing the focal length of the lenses and the crop factor of the camera, the focal length f can be calculated. Finally, it is assumed that $T_x$ is 1 so the scale will depend on the real value of $T_x$.

In conclusion, it is convenient to use a 3D calibration object with a known shape and easy to represent it by a mathematical function to get the points that forms the object. In order to determine the best input values of the function, an optimization algorithm can be implemented in which the objective is to minimize the MSE between the points of the calibration object obtained by the reconstruction code and the geometric function.

# Chapter 4

# Experiments on VKI Plasmatron

Three experiments were carried out with different samples inside the test bench. The stereo photogrammetry technique to measure the ablation in the VKI Plasmatron is in development, so it is necessary to figure out how the cameras respond under the brightness conditions of the plasma. Moreover, which camera arrangement is optimal to take pictures of the sample taking into account the position of the windows and dealing with other measuring devices. Additionally, it is important to check how the triggering system works under the electromagnetic field and also the acquisition frequency to capture the evolution of the surface properly or possible interferences of the electromagnetic field with the cameras.

In each test, a different sample was mounted. This is important because depending on the material, the ablation rate, the luminosity condition and the VKI Plasmatron power will be different. It is important to reproduce different conditions in order to create an expertise of the camera settings with different conditions valid for future experiments with similar conditions.

## 4.1   P50 Cork Sample Test

### 4.1.1   Sample

The cork sample mounted on the VKI Plasmatron is made of a cylinder and a tangent hemisphere (Figure 4.1). Its dimensions are shown on the Table 4.1. The material is P50 cork but this sample represents the shape of a typical test sample used during the ablation test of reals materials (Section 4.3). Half of the cork sample was painted with lines from the tip to the end split each 45°. Also, it was divided by lines in the perpendicular direction. This was done to have more feature points hence improving the accuracy of the calibration.
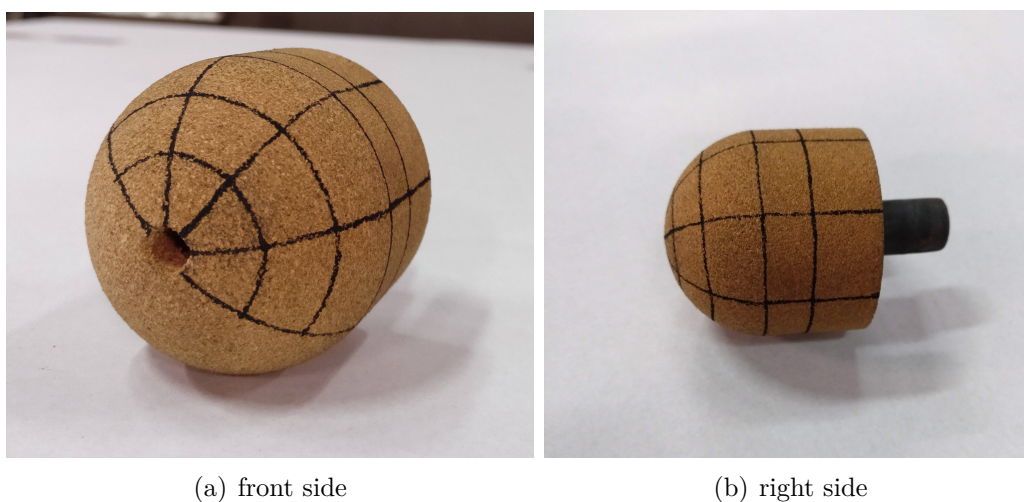
(a) front side　　　　　　　　　　　(b) right side

Figure 4.1: Cork sample used for the experiment prepared to be mounted in the VKI Plasmatron

| Parts | Height (cm) | Diameter (cm) |
|---|---|---|
| Cylinder | 2.5 | 5 |
| Hemisphere | - | 5 |

Tabla 4.1: Dimensions of the cork sample tested

## 4.1.2　Set up

In this part of the experiment was necessary to figure out the best position for the cameras in order to see the sample with the most common feature points between cameras. Although the VKI Plasmatron has 6 windows, there are others cameras and measuring equipment on the other windows. For this experiment, the Prosilica GT cameras were mounted on the right side window (GT2000) at a range of 90 cm and the front up right window (GT2050) at a range of 120 cm as it is showed in Figure 4.3. With this camera arrangement, there is a view perpendicular to the sample and other one, oblique of the up-left part of the sample as it can be seen in Figure 4.5. The lenses used for both cameras have a focal length of 50 mm.

The other camera used was placed on the right window behind the Prosilica (Figure 4.4), so the image was a perpendicular view of the sample. It should be noted that only one of this type of cameras was used because the triggering system to synchronize them cameras was not ready during this test but still one of the purpose was to check how this camera worked under the luminosity conditions of the experiment. This camera
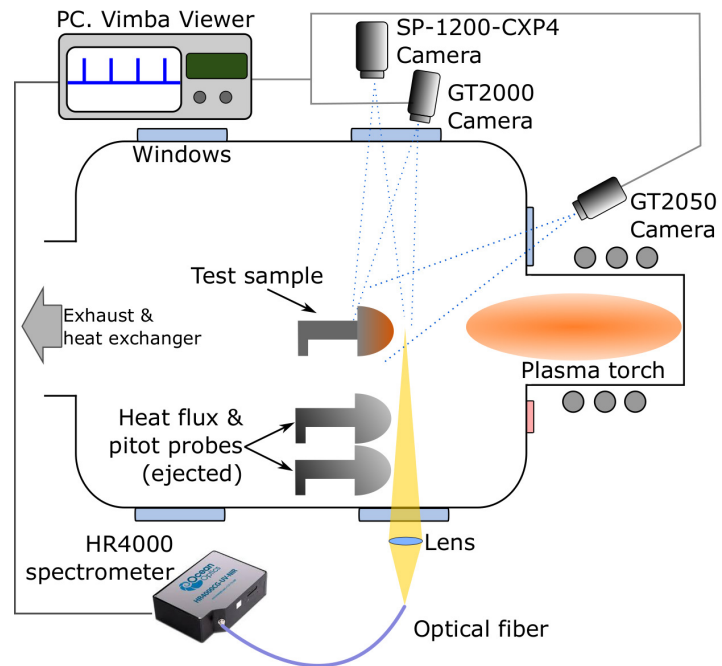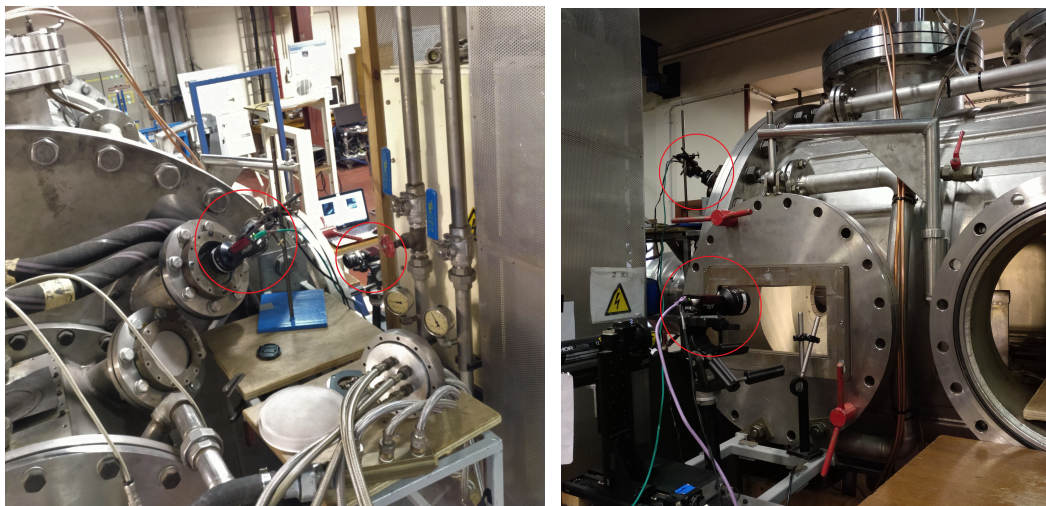
Figure 4.2: Scheme of the set up used during the P50 cork tests



(a) Front view

(b) Side view

Figure 4.3: Cameras placed on the Plasmatron windows during the P50 cork tests.

was mounted the objective of 105 mm of focal length.

The aperture of the lenses were the minimum possible in all of them because the brightness conditions during the experiment can saturate the sensor of the cameras. For the 50 mm lens the maximum F-number is 22 and for the 105 mm is 32 (Section 4.2).
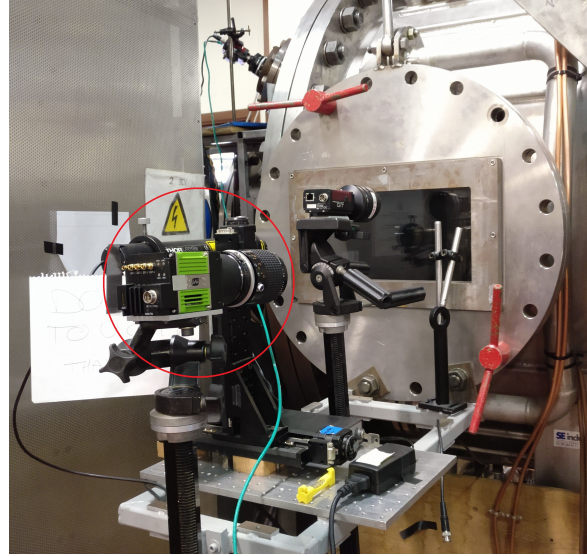


Figure 4.4: Camera SP-12000-CXP4 mounted during the experiment

| Camera | GT 2000 | GT 2050 | SP-12000-CXP4 |
|---|---|---|---|
| Focal length (mm) | 50 | 50 | 105 |
| F-number | 22 | 22 | 32 |
| Distance Sample (cm) | 120 | 90 | 140 |
| Resolution | 1088(H)x1088(V) | 1088(H)x1088(V) | 2048(H)x2048(V) |

Tabla 4.2: Configuration of the cameras during the experiment

### 4.1.3 Results

The results of this test will be presented in two parts. The first part shows the results with the Plasmatron turned off and the second part the results of the tests with the Plasmatron turned on.

**Plasma off Test**

This part of the experiment consists of taking pictures of the cork sample mounted inside the Plasmatron in order to make the camera calibration. It is important to configure

the camera parameters with the real test values in order to make the calibration with the same camera parameters that the experiment.



(a) Front View                                     (b) Side View

Figure 4.5: Views of the Cork sample inside the Plasmatron

The exposure time is $800\,000$ ms because the aperture of the cameras is set at the minimum value of the lenses and the light conditions with the Plasmatron turned off are very dark. The exposure time is the only parameter that can be changed without affecting the calibration.
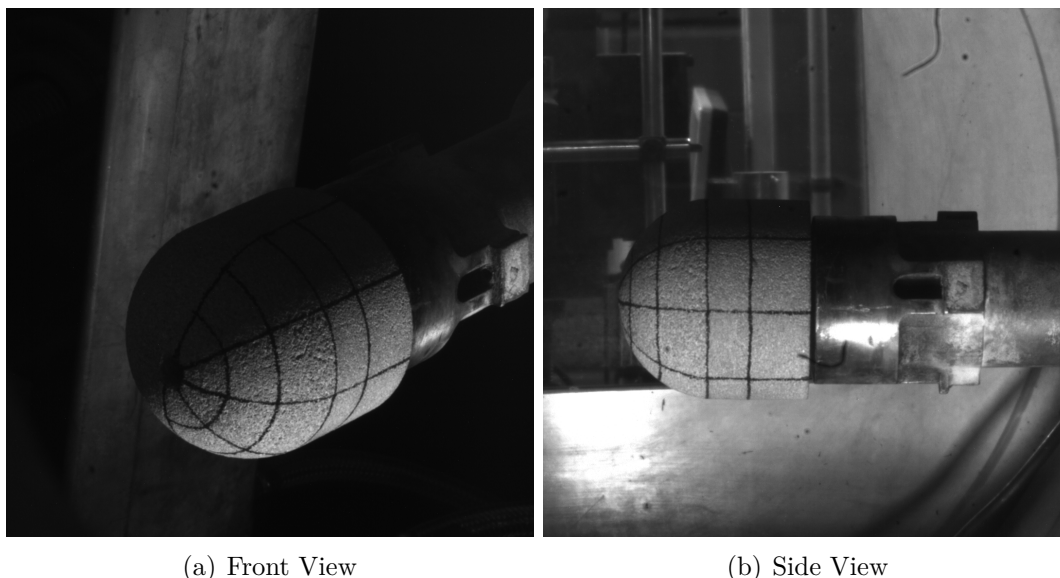
**Plasma on Test**

The Table 4.3 shows the parameters and the results of each experiment. The VKI Plasmatron power in the majority of the test is the nominal value and increases during the last test in order reproduce different test condition to check how the cameras respond to higher light conditions. There are two successful test which the cameras are synchronized and the pictures were taken with the correct exposition.

The exposure time was configured to the minimum value in both cameras to avoid damaging the sensor of them because there was no previous knowledge about the response of the cameras under the brightness conditions. Once the plasma was started, the value was increasing.

Figures 4.6, 4.7, 4.8, 4.9 represent an example of the pictures taken during each test.

| Test | Power (kW) | Exp. time ($\mu$s) | Recorded Pictures | Result |
|------|-----------|--------------------|-------------------|--------|
| Test 1 | 120 | 50-500 | - | Locked PC. Failed |
| Test 2 | 120 | 200 | 30 - 30 | Asynchronous cameras |
| Test 3 | 120 | 200 | 30 - 0 | Failed |
| Test 4 | 120 | 200 | 30 - 30 | Successful |
| Test 5 | 200 | 50 | 30 - 30 | Successful |

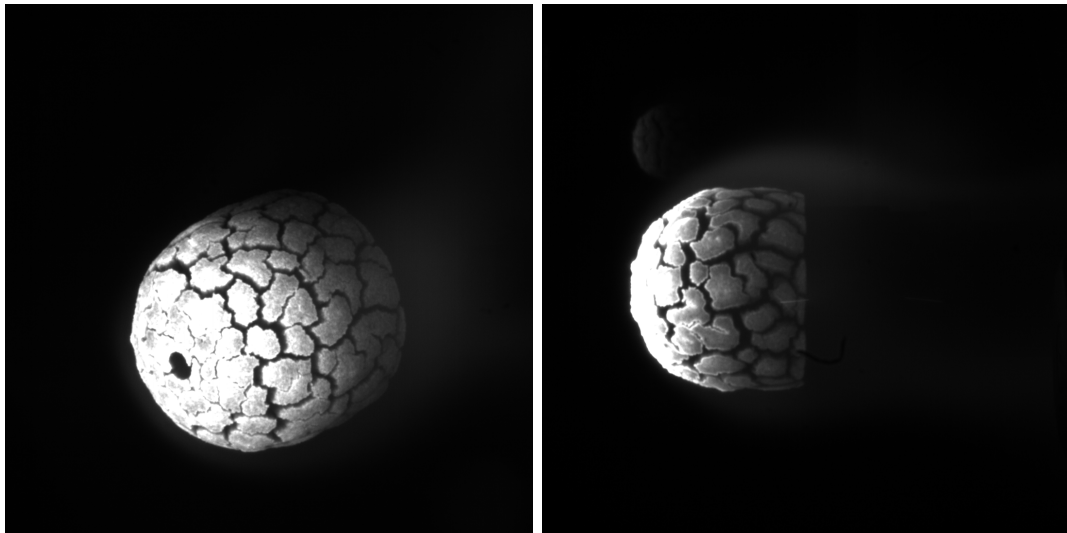Tabla 4.3: Summary of the experiments with the Prosilica cameras



Figure 4.6: Test 2. Testing the cork sample inside the Plasmatron. Pictures taken at different time

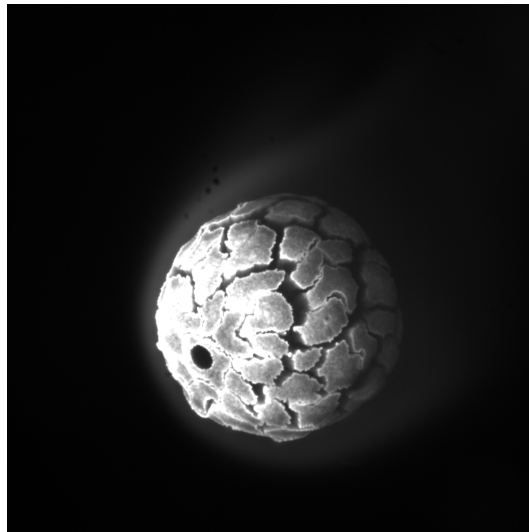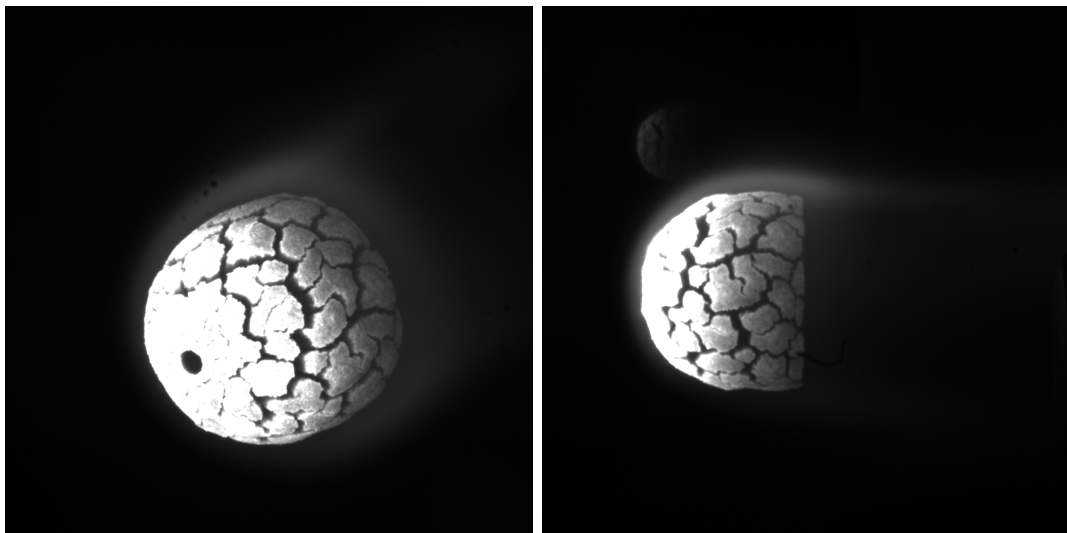Figure 4.7: Test3. Testing the cork sample inside the Plasmatron. No recorded pictures from the right side camera



(a)                                                        (b)

Figure 4.8: Test 4. Testing the cork sample inside the Plasmatron.

(a) (b)
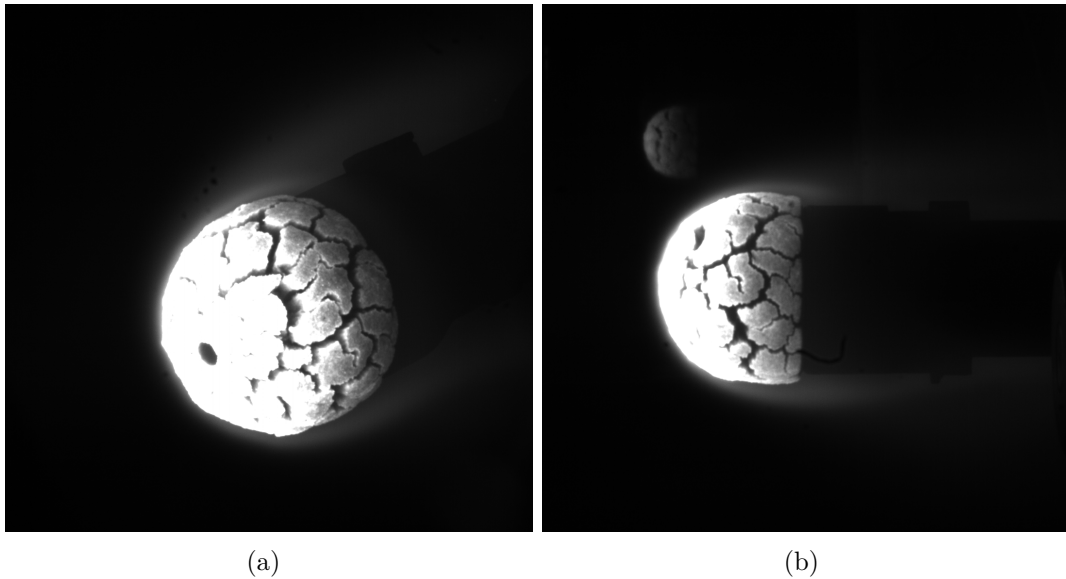
Figure 4.9: Test 5. Testing the cork sample inside the Plasmatron at high energy

The experiments with a fail result are due to a problem with the triggering system because the cameras were not well synchronized. Also, the computer is working under a high electromagnetic field emitted by the electric generator so it can get locked and stop acquiring pictures.

Finally, the experimental part was successful because there are two test which pictures taken. Also, they are synchronized and have a good quality to recognize the feature points by the code. However, the problem with these pictures is that the angle between cameras is too large to apply the reconstruction code. It is because the common points are difficult to recognize automatically in both pictures by the code.

In order to check how the SP-12000-CXP4 camera works and records images under the Plasmatron conditions, some pictures were taken and they are shown in the Figure 4.10. The resolution in this pictures is higher than the other pictures but the differences are not really substantial. The reconstruction code can not be applied because there is only one picture with this camera.

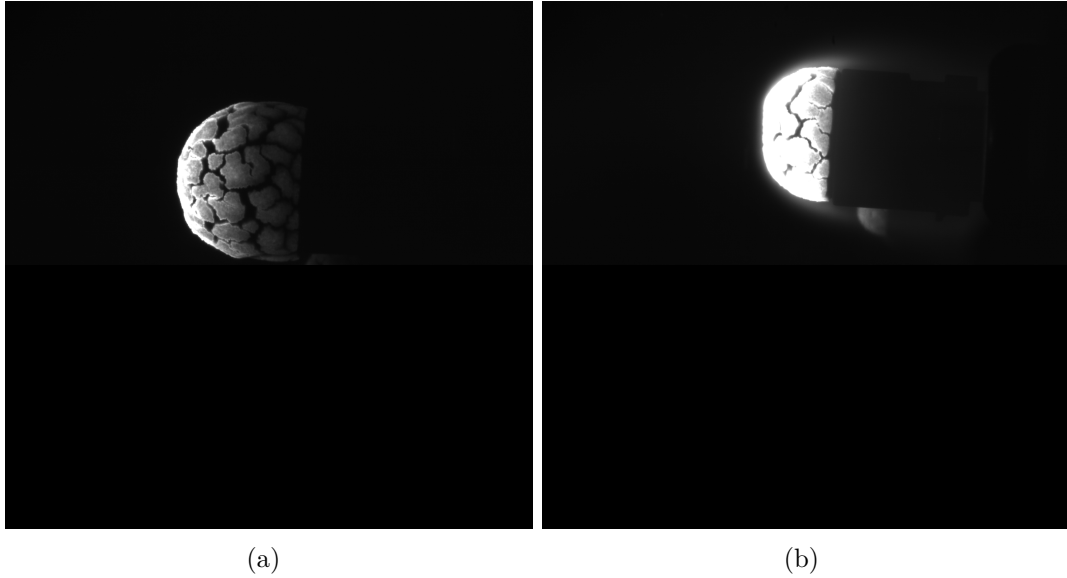Figure 4.10: Test camera SP-12000-CXP4. Pictures of the cork sample at different time.

## 4.2 Graphite Sample Test

### 4.2.1 Sample

In this experiment, a graphite sample has been tested in the VKI Plasmatron in order to study the ablation process of this material. This material has a smooth surface which hinders the recognition of feature points in the pictures. This sample is made of a cylinder and two hemispheres on each side. The dimensions of the cylinder and the hemispheres that made up the total sample are shown on the Table 4.4.

| Parts | Length (mm) | Diameter (mm) |
|-------------|-------------|---------------|
| Cylinder | 50 | 70.8 |
| Semi sphere | - | 70.8 |

Tabla 4.4: Dimensions of the graphite sample tested in the Plasmatron

This experiment is divided in two parts. The first part, the sample is mounted horizontally and there are two different tests in which the VKI Plasmatron power was increasing (Figure 4.11). The second part, the sample is mounted vertically and there is only one test. Figure 4.12 shows the sample after the first part of the experiment prepared to be mounted to complete the second part of the experiment.

(a) front side                    (b) right side

Figure 4.11: Graphite sample used for the experiment prepared to be mounted in the Plasmatron in the first part of the experiment. Courtesy of Maxim Laeveren.



(a) front side                    (b) right side

Figure 4.12: Graphite sample used for the experiment prepared to be mounted in the Plasmatron in the second part of the experiment. Courtesy of Maxim Laeveren.

## 4.2.2 Cameras Set up

Related with the position of the cameras, in the first part of experiment both of them have been placed on the same side of the VKI Plasmatron, near the right window (Figure 4.14). Unlike the previous experiment with the cork sample, in this one, other measuring equipment was mounted so there were not more available windows to place the cameras. With this configuration, the angle between cameras is small enough in order to apply the reconstruction code. The problem of this configuration is that only the right side of the sample can be defined, because is the only visible part. However, there will be a high precision because the views from both cameras are quite close and there are more feature points in common to be recognized by the reconstruction software. Table 4.5 shows the configuration of both cameras for this experiment. Note that the focal length of the lenses is higher than the previous experiment because the distance from the cameras has increased.

This experiment takes part of other project carried out at VKI Plasmatron but it was a good opportunity to get more experience taking pictures during real tests in the VKI Plasmatron, also with a different material and different conditions.
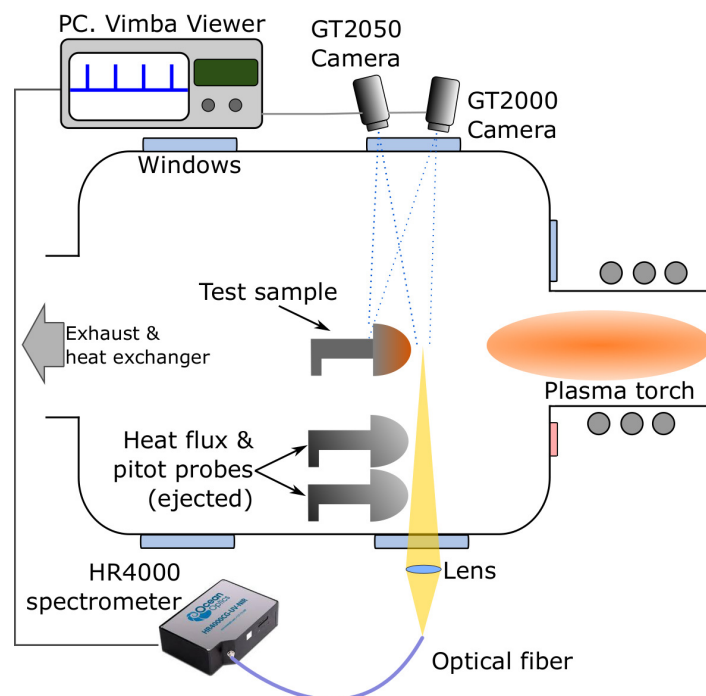
Figure 4.13: Scheme of the set up for the first part of the graphite experiment
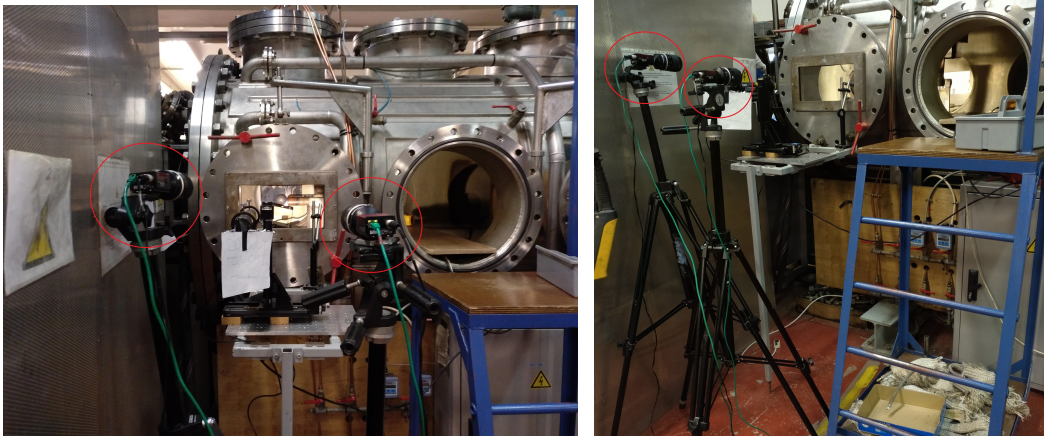
Figure 4.14: Cameras placed on the Plasmatron windows during the first part of the experiment

| Camera | GT 2000 | GT 2050 |
|---|---|---|
| Focal length (mm) | 105 | 105 |
| F-number | 32 | 32 |
| Distance Sample (cm) | 150 | 150 |
| Position | right | left |
| Resolution | 1088(H)x1088(V) | 1088(H)x1088(V) |

Tabla 4.5: Configuration of the cameras during the first part of the experiment

In the second part of the experiment, the cameras were mounted on the left up window and on the right side window as is shown in the Figure 4.16. The characteristics of the cameras are shown in the Table 4.6. The focal length, in this part of the experiment, is lower than the first part because the cameras are closer to the Plasmatron. In this case, the configuration is far away from the best possible because both views barely share common points. Apart from having the problem with the other measuring equipment, the reason to try different configurations in each experiment is to check how the cameras work from each window and figure the best configuration out for the reconstruction software.
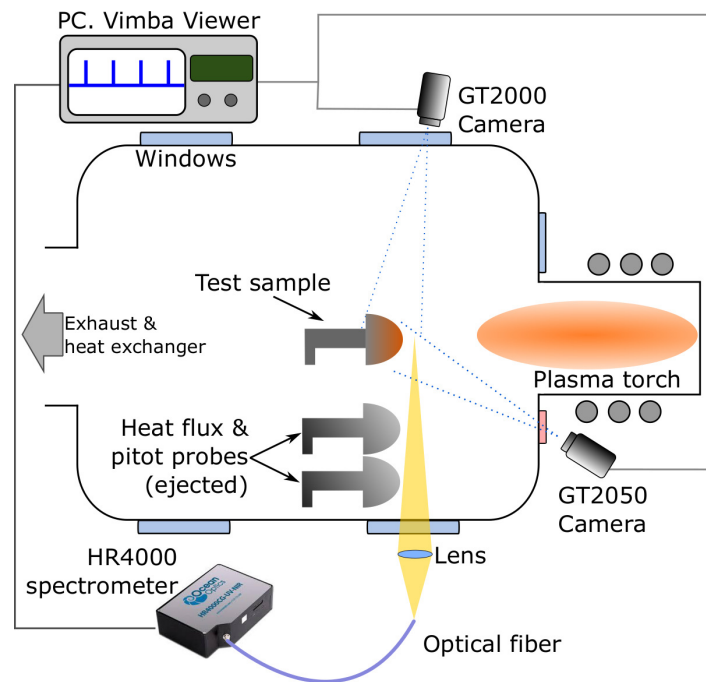
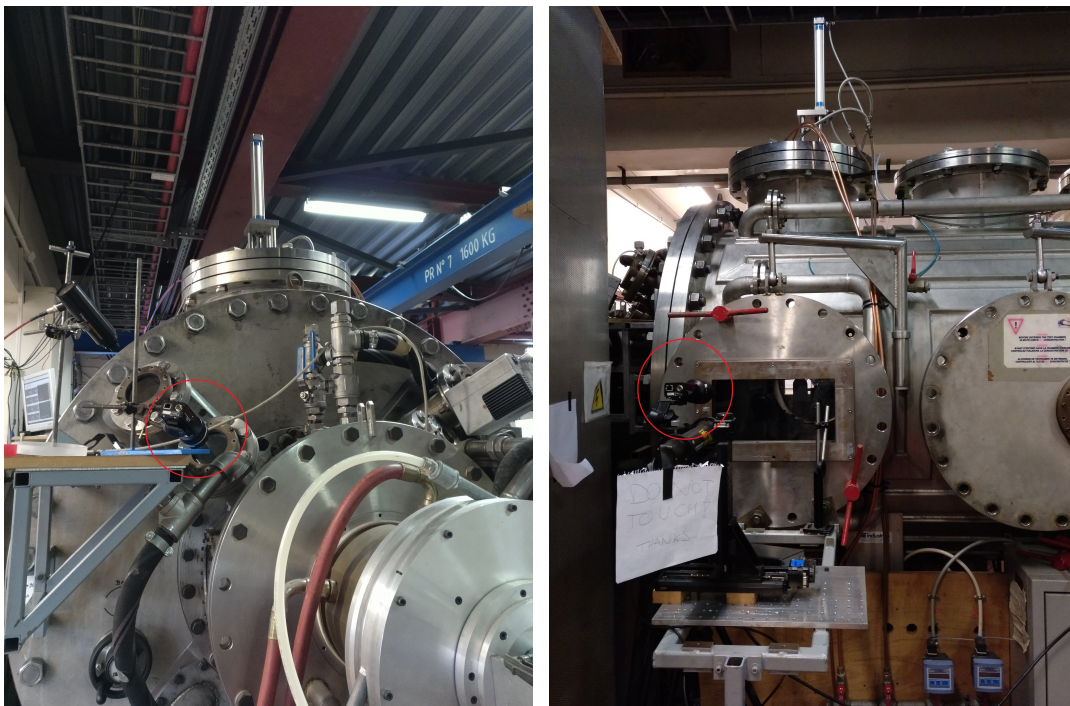Figure 4.15: Scheme of the set up for the second part of the graphite experiment



Figure 4.16: Cameras placed on the Plasmatron windows during the second part of the experiment

| Camera | GT 2000 | GT 2050 |
|---|---|---|
| Focal length (mm) | 50 | 50 |
| F-number | 22 | 22 |
| Distance Sample (cm) | 90 | 120 |
| Position | left | right |
| Resolution | 1088(H)x1088(V) | 1088(H)x1088(V) |

Tabla 4.6: Configuration of the cameras during the second part of the experiment

### 4.2.3 Results

**Plasma off Test**

In this test, the pictures of the sample were taken in order to reconstruct the geometry when the Plasmatron is turned off. It can be seen in the Figure 4.17 there are no feature points easy to recognise by the software in both pictures in order to reconstruct the geometry. This is because the surface of the sample is very smooth as commented before.
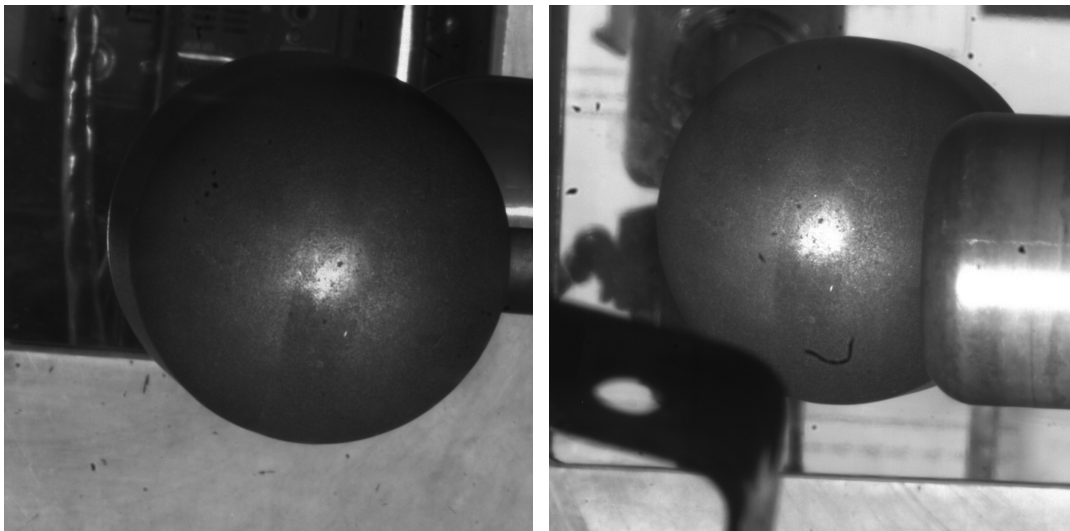


Figure 4.17: Graphite sample inside the Plasmatron from both cameras in the first part.

More feature points are observed on the surface (Figure 4.18) because it ablated during the previous experiment. This is advantageous because the software requires such feature points to reconstruct the sample.
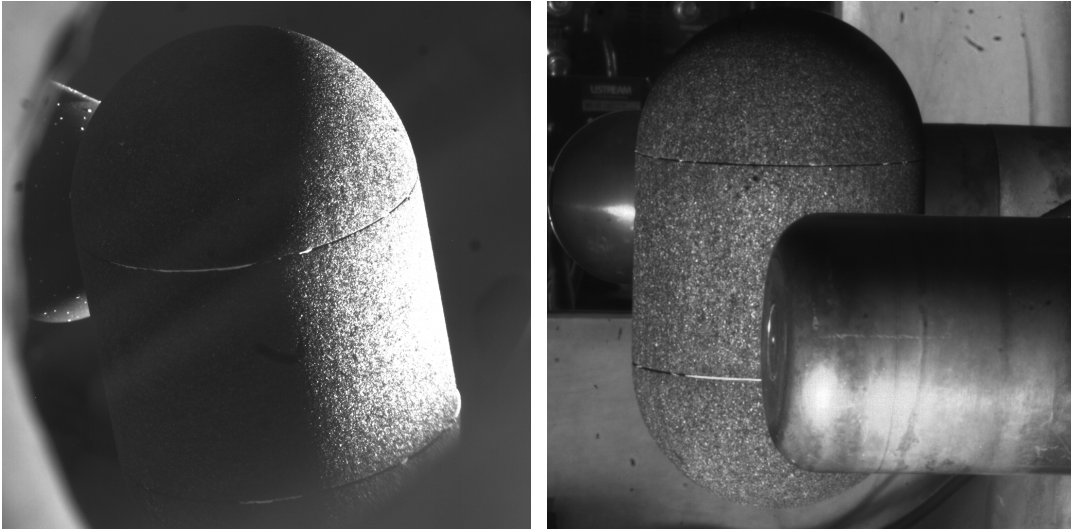
Figure 4.18: Graphite sample inside the Plasmatron from both cameras in the first part.

**Plasma on test**

This experiment can be split in three parts in which the power of the Plasmatron was increased (Table 4.7). While in test 1 no pictures were properly acquired because the exposure time was being adjusted, in tests 2 and 3 this issue was solved and pictures were recorded.

Figures 4.19 and 4.20 show the graphite sample inside the Plasmatron during the first part of the experiment. On the leading edge of the sample, the pictures are over-saturated because the exposure time was too high. Moreover, this sample does not have feature points and the shape smooth. The duration of this experiment was very short and the exposure time used for the previous experiment of the cork sample was not useful for this test because the heat flux is different and also the brightness.

| Test | Power (kW) | Exp. time ($\mu$s) | Sample | Recorded Pict. | Result |
|------|-----------|--------------------|--------|----------------|--------|
| Test 1 | 120 | 1000 | Horizontal | - | Failed |
| Test 2 | 161 | 800 | Horizontal | 2 x (10 - 10) | over-satur. Pict. |
| Test 3 | 227 | 500 | Vertical | 4+5 - 4+5 | over-satur. Pict. |

Tabla 4.7: Summary of the experiments of the graphite sample with the Prosilica cameras

There are not many feature points easily to recognize by the software (Figures 4.21 and 4.22) because the pictures taken are over-saturated too.
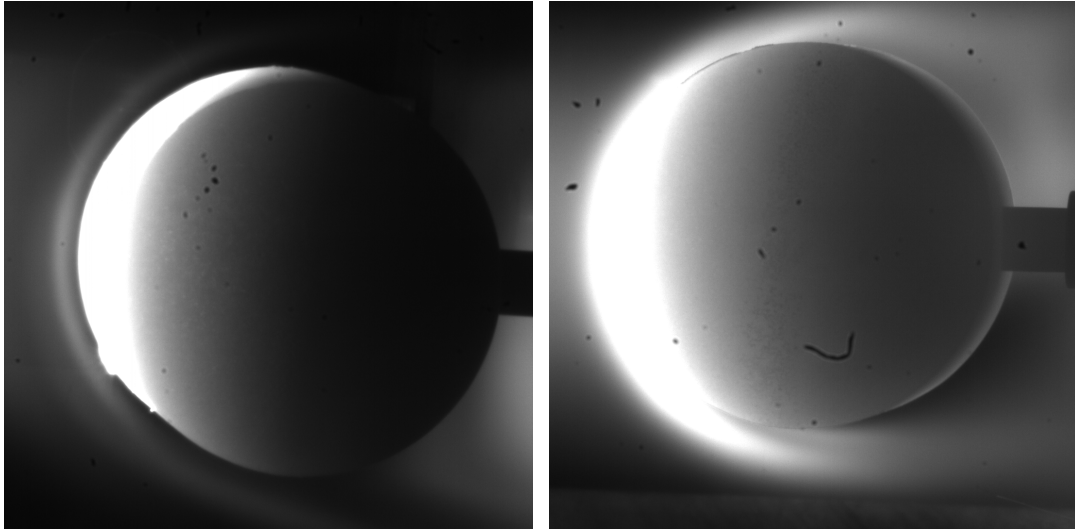
Figure 4.19: Test 2. First set of pictures. Graphite sample testing in the Plasmatron
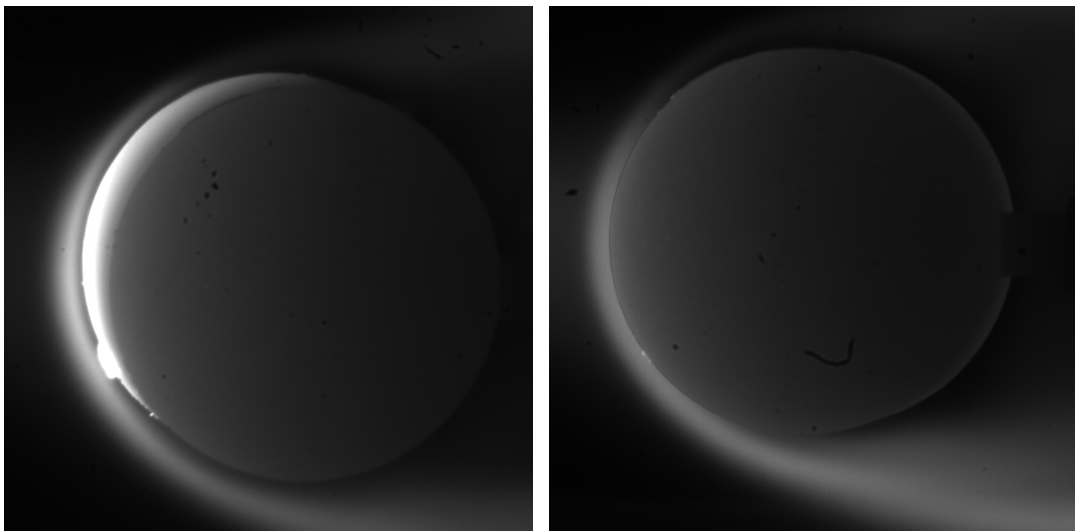


Figure 4.20: Test 2. Second set of pictures. Graphite sample testing in the Plasmatron when the flow was turned off and the sample was red hot.
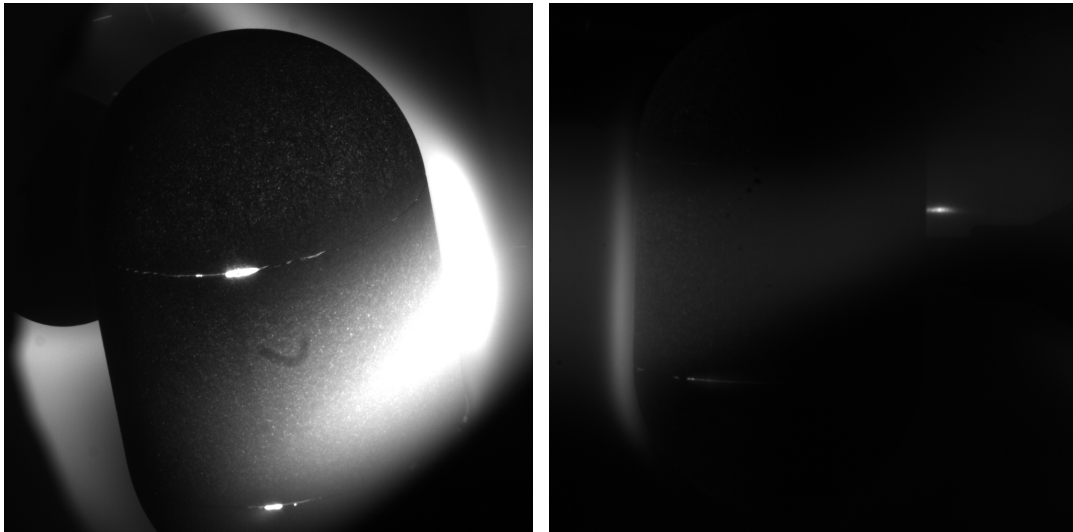
Figure 4.21: Test 3. First set of pictures. Graphite sample testing in the Plasmatron
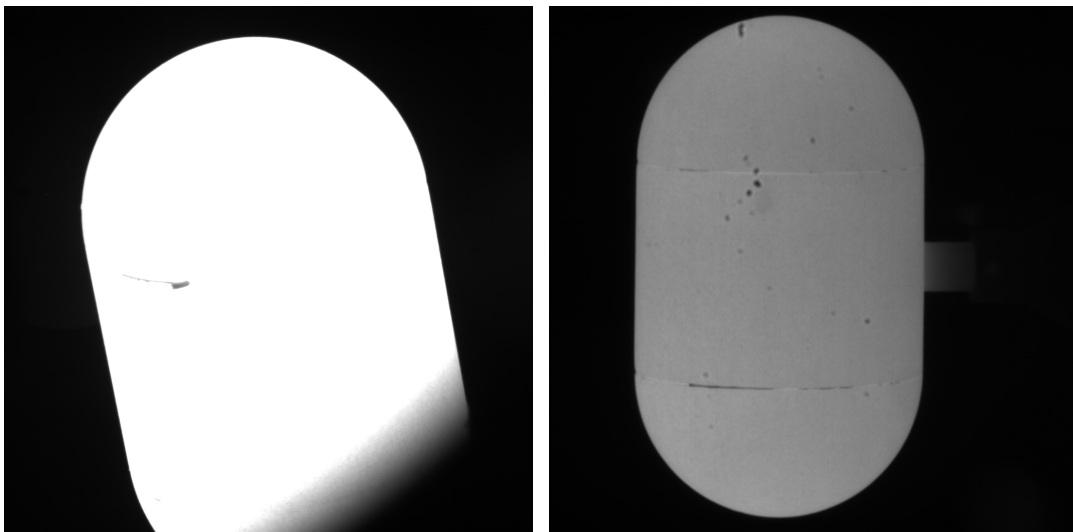


Figure 4.22: Test 3. First set of pictures. Graphite sample testing in the Plasmatron. The plasma flow was over but the graphite sample was red hot.

To conclude, the ablation process of this kind of material does not present cracks and feature points to recognize as easily as the experiment of the cork sample. Additionally, the pictures are over-saturated so it makes more difficult the reconstruction of the sample with the pictures taken.

# 4.3 ZURAM® Test

## 4.3.1 Sample

This is the last ablation experiment carried out in this project. The sample tested is ZURAM® (Section 3.3.3) and it has the same shape and dimensions as the cork sample (Table 4.8). In this test two states of the material will be studied, which are virgin and pyrolysed. They are shown in Figure 4.23 and Figure 4.24.



(a) side　　　　　　　　　　　　　　(b) front

Figure 4.23: Virgin ZURAM® sample used for the experiment prepared to be mounted and mounted in the VKI Plasmatron. Courtesy of Bernd Helber.
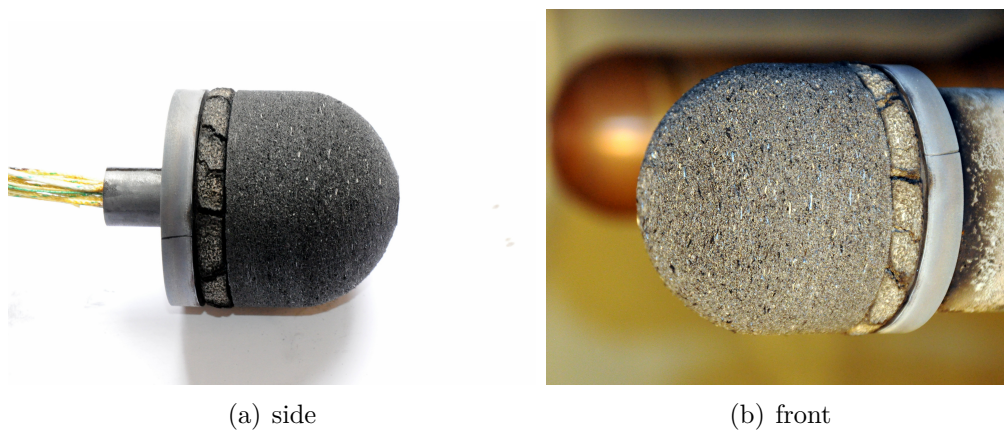


(a) side　　　　　　　　　　　　　　(b) front

Figure 4.24: Pyrolyzed ZURAM® Sample used for the experiment prepared to be mounted and mounted in the VKI Plasmatron. Courtesy of Bernd Helber.

| Parts | Height (cm) | Diameter (cm) |
|-------|-------------|---------------|
| Cylinder | 2.5 | 5 |
| Hemisphere | - | 5 |

Tabla 4.8: Dimensions of the ZURAM® sample tested

## 4.3.2 Set up

The camera set up (Figure 4.26) is almost the same as the cork sample experiment but it presents two differences. The GT 2050 camera was placed on the front up right window. As there are two, the one used is the lower one. From this window, the camera has to be placed oblique in order to have a good view of the sample. It generates a problem because the glass can introduce reflections and distortions in the pictures. The other difference is the lenses mounted on the cameras, because the focal length is higher than the other test, 105 mm versus 55 mm. With this focal length, the frame of the pictures is mostly occupied by the sample, which means that there are more pixels that contain information about the sample. In this case, as the objectives are different, its F-number is higher than the other objectives of 55 mm, so the values of the exposure time will be affected and the ones used on the other experiment will not be valid. The other parameters like the resolution, distance to the sample, etc. are shown in Table 4.9.
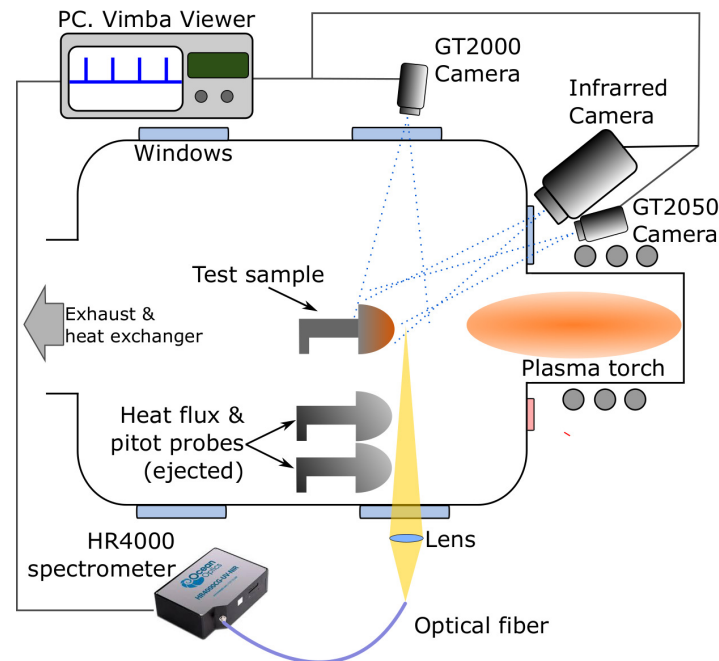


Figure 4.25: Scheme of the set up mounted on the ZURAM® experiment

| Camera | GT 2000 | GT 2050 |
|---|---|---|
| Focal length (mm) | 105 | 105 |
| F-number | 32 | 32 |
| Distance Sample (cm) | 120 | 120 |
| Position | left | right |
| Resolution | 1088(H)x1088(V) | 1088(H)x1088(V) |

Tabla 4.9: Configuration of the cameras during the second part of the experiment



(a) front side (b) right side
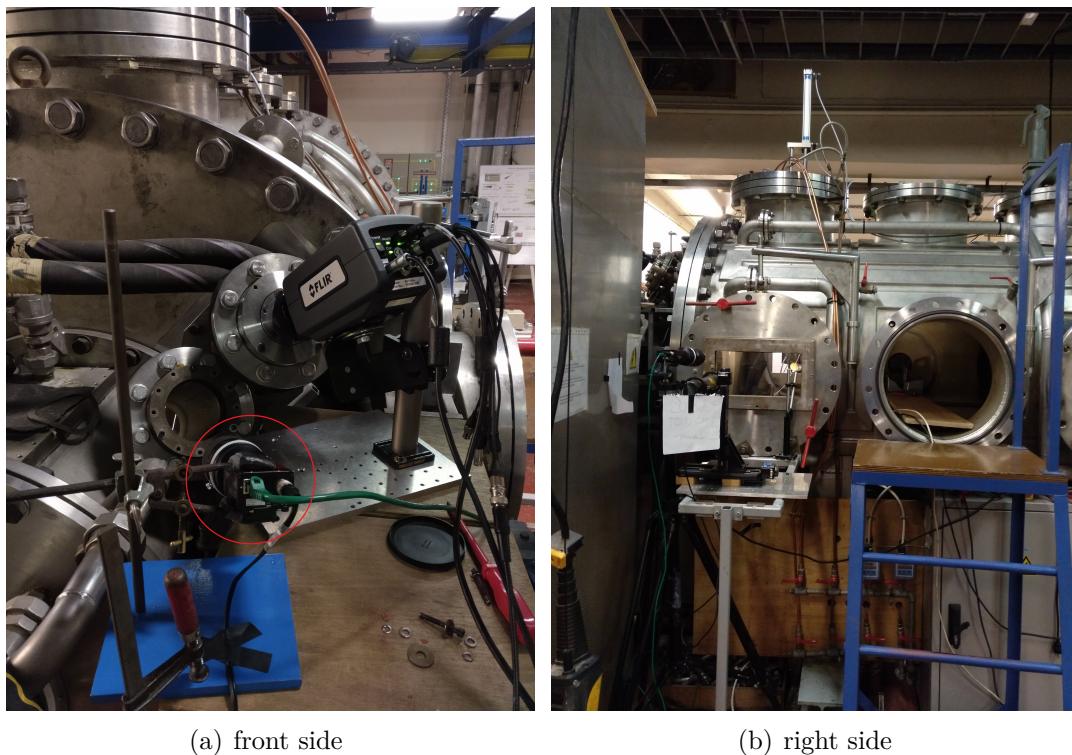
Figure 4.26: Set up mounted for the ZURAM® ablation experiments. The camera of the front side is placed on the lower window unlike previous experiments.

### 4.3.3 Results

**Plasma off test**

Figures 4.27 and 4.28 shows the views of the sample from the two cameras at the beginning of the two experiments. The pyrolyzed sample presents more features points so it would be easier for the reconstruction code in order to recognize these points to

manage the 3D reconstruction.



(a)                                            (b)

Figure 4.27: Test 2. Views of virgin ZURAM® sample mounted in the VKI Plasmatron with the plasma off.



(a)                                            (b)

Figure 4.28: Test 3. Views of pyrolyzed ZURAM® sample mounted in the VKI Plasmatron with the plasma off.

**Plasma on test**

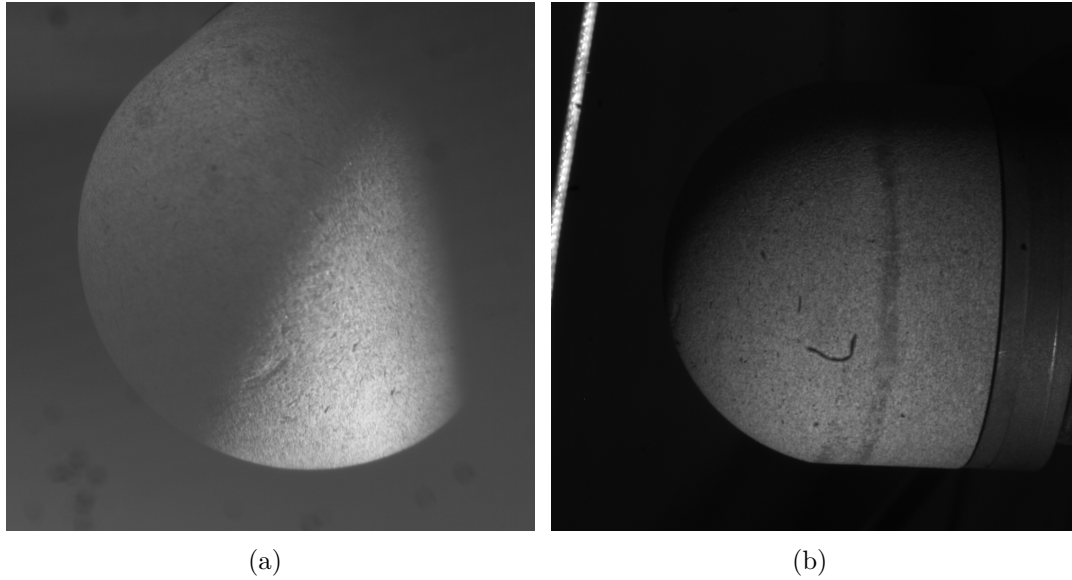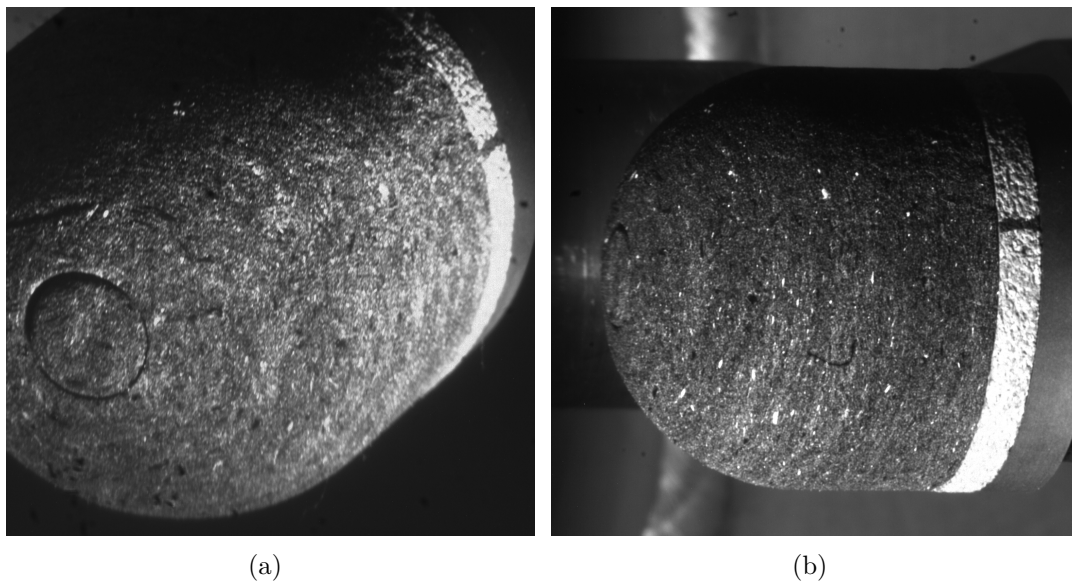This experiment can be split in three parts, in which two of them the sample is the virgin one and the other is the pyrolyzed (Table 4.10). During the test 2 was not possible to take any pictures because the exposure time needed to be configured previously. Depending on the heat flux, the value of the exposure time is different.

| Test | Sample | Heat flux (MW/$m^2$) | Exp. time ($\mu$s) | Num. Pict. | Result |
|------|--------|-----------------------|---------------------|-------------|---------------|
| Test 2 | Virgin | 0.29 | - | - | - |
| Test 3 | Pyrolyzed | 2.5 | 300 | - 30 | over-satur. |
| Test 4 | Virgin | 0.29 | 1500-2200 | 4 x (5 - 5) | under-satur. |

Tabla 4.10: Summary of the experiments of ZURAM® sample with the Prosilica cameras

Figure 4.29 shows a picture taken during the test 3. There is only one picture because the cameras were not well synchronized. Also the picture is over-saturated because the exposure time set was too high for that heat flux. However, the duration of the experiment was 30 s so there was no chance to change it.
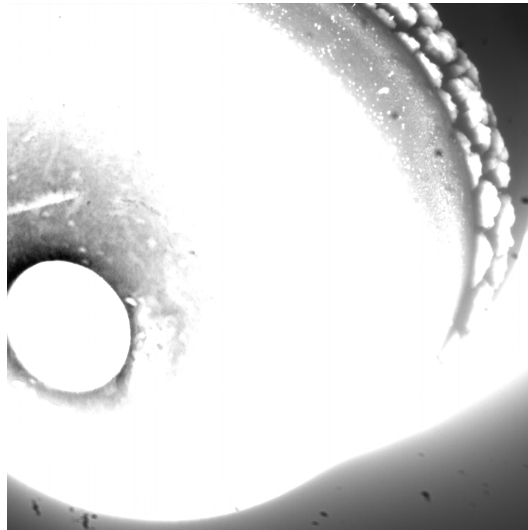


Figure 4.29: Test 3. Front view of the ZURAM® sample during the ablation test.

Figures 4.30 and 4.31 show the pictures taken during test 4. It can be seen that in the first pair of images, the front part of the sample is over-saturated while the back part is sub-saturated. The other images present a different exposition, so it means that the exposure time should have been different in two cameras. In the other set of pictures, the exposure time was set in a lower value and the pictures in that case were sub-saturated. This may be because the camera is not positioned orthogonal to the window and it can introduce reflections or other light conditions.

(a)                                    (b)

Figure 4.30: Test 4.1. ZURAM® sample during the ablation experiment. Exposure time 2000 $\mu$s



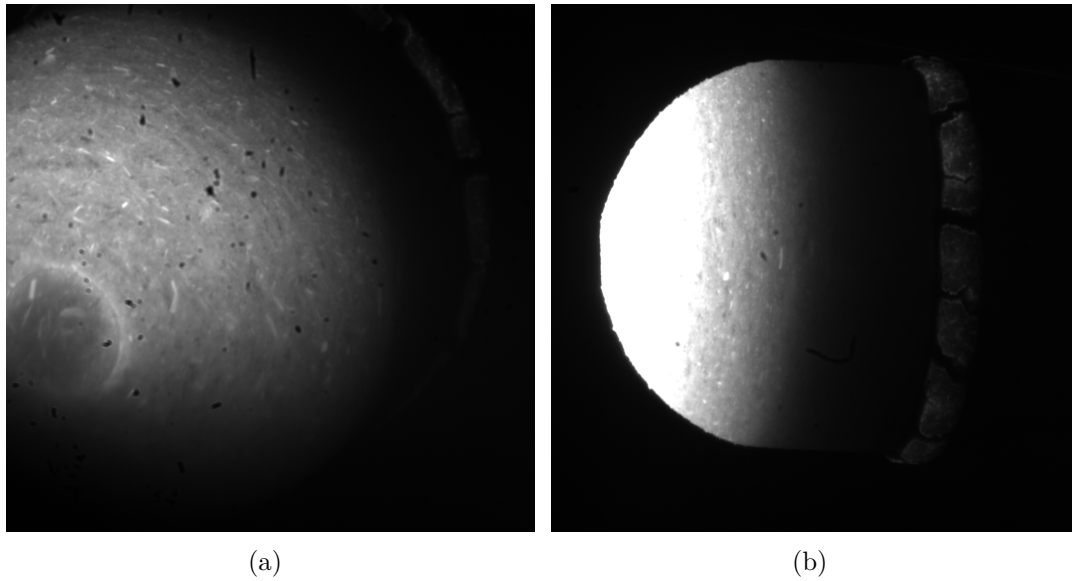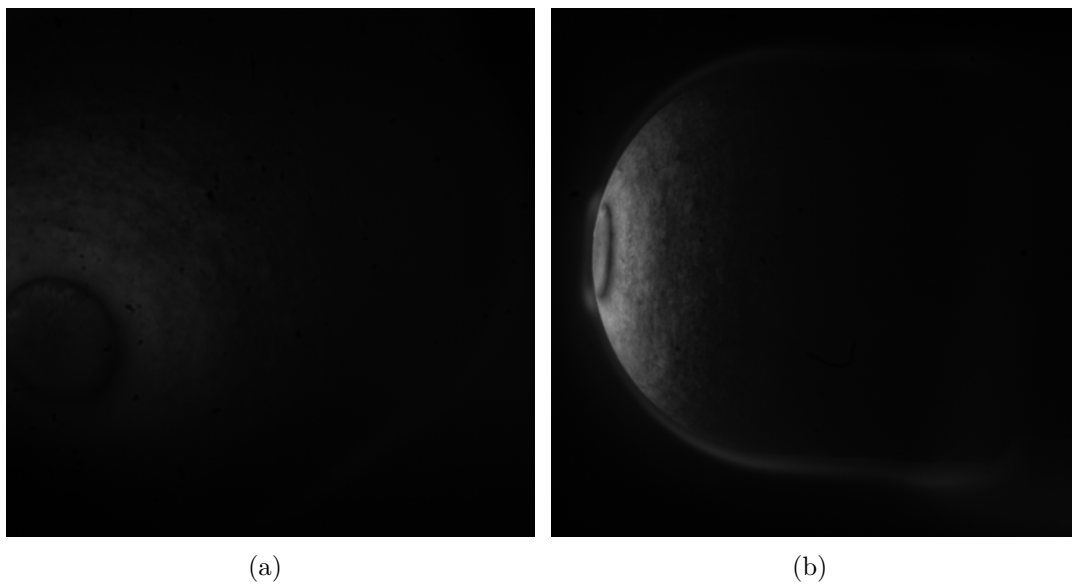(a)                                    (b)

Figure 4.31: Test 4.2. ZURAM® sample during the ablation experiment. Exposure time 2500 $\mu$s

# Chapter 5

# 3D reconstruction of a Sample

Section 3.5 explains how the reconstruction code works theoretically. This section shows how the reconstruction code manages the calibration method, the optimization algorithm and finally the results of the reconstruction mesh of the pictures taken.

As said before, this reconstruction code uses a known geometry, instead of a calibration pattern like a chessboard in order to calibrate the cameras. In this project, the calibration object is formed by a hemisphere and a cylinder. The steps of the calibration are two: 1) reproduce the 3D calibration object by a mathematical function. 2) use the optimization algorithm developed to calculate the parameters which minimizes the MSE. Finally, with the value of the input parameters, it is foreseen to reconstruct other similar object with high precision.

The camera arrangement consists of the two cameras placed horizontally and separated an angle of 12 degrees (Figure 5.1). The camera settings are explained in Table 5.1. The F-number and the exposure time are configured for a typical room light conditions. This set up is outside and apart from the test bench so there are a lot of degree of freedom to place the cameras. They are placed at the same distance to the sample, with a small angle and horizontally in order to have the most ideal configuration to maximize the common points between pictures.

The pictures of the sample used as input of the reconstruction code are shown in Figure 5.2. There is a lot of feature points in the surface easily to recognize by the code, there is a good contrast with the background, both pictures are very similar and the sample is placed in the middle of the frame in order to facilitate the recognition of the common points.

After the execution of the code with each optimization method, the results obtained are presented in Table 5.2. The three methods reach the same solution of the MSE although the input parameters are not exactly the same. Comparing the methods taking into account the number of iterations, the lowest one has been achieved with

Figure 5.1: Set up used for the test apart from the test bench to apply the reconstruction code.

| Camera | GT 2000 | GT 2050 |
|---|---|---|
| Focal length (mm) | 50 | 50 |
| F-number | 4 | 4 |
| Exposure time ($\mu$s) | 100000 | 100000 |
| Distance Sample (cm) | 60 | 60 |
| Resolution | 2048(H)x1088(V) | 2048(H)x1088(V) |

Tabla 5.1: Configuration of the cameras during the experiment in a laboratory apart from the test bench
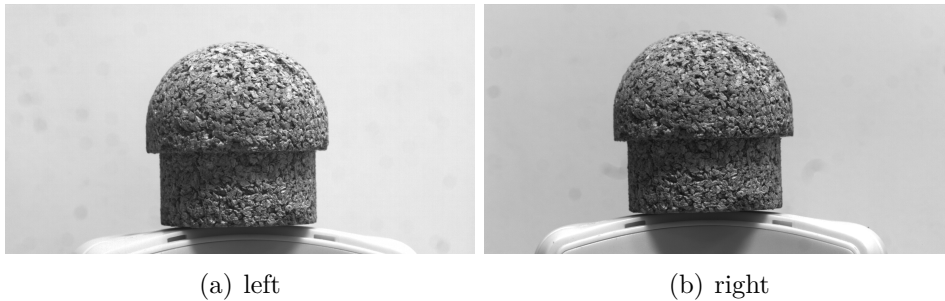


(a) left        (b) right

Figure 5.2: Cork sample used for the optimization algorithm

"conmin_frcg" method. This is because it consist a local optimizer and the initial solution proposed is very close to the final solution previously calculated in the sensitivity analysis. "Soga" method has the largest number of iterations because it is a global method and the solution is calculated by random values within a range.

For this specific case, the best method is "conmin_frcg" because as said before, the initial solution, calculated in the sensitivity analysis [20], is close to the final one. However, in case that there is no any estimation of the initial solution, the recommended method is "soga" because it calculates some points during each step of the iteration process.

| Method | Iterations | focal length | num disp | min disp | MSE |
|---|---|---|---|---|---|
| conmin_frcg | 16 | 5.256 | 208 | -15 | 26.742 |
| asynch_pattern_search | 53 | 5.674 | 224 | -15 | 26.867 |
| soga | 160 | 5.488 | 208 | -13 | 29.636 |

Tabla 5.2: Results of the MSE calculated by each optimization method with the pictures taken of the sample outside the VKI Plasmatron.
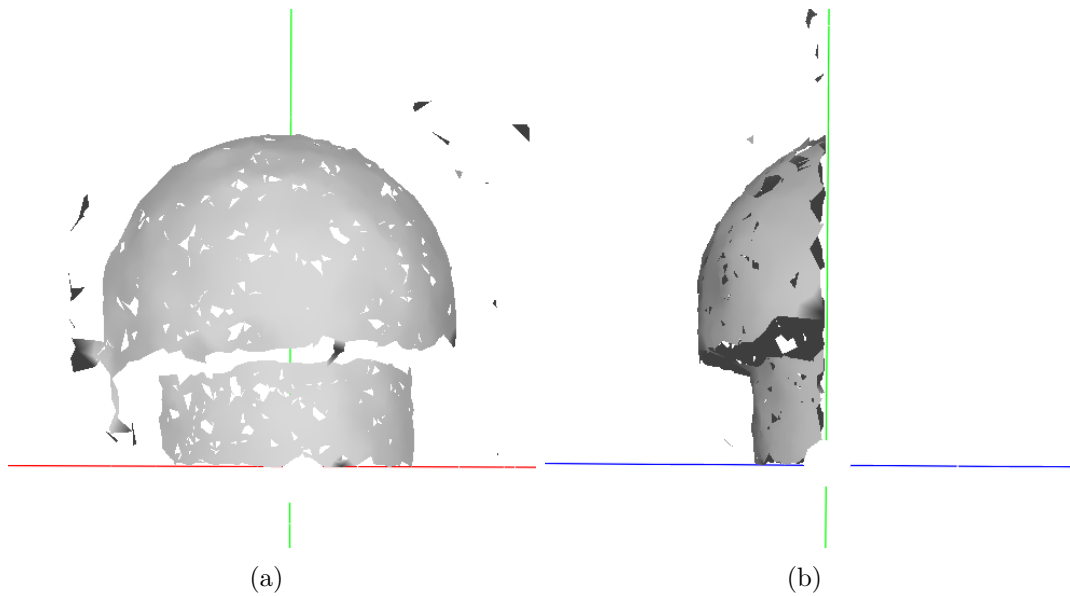


(a)          (b)

Figure 5.3: Reconstruction of the sample applying the solution of "conmin_frcg" method.
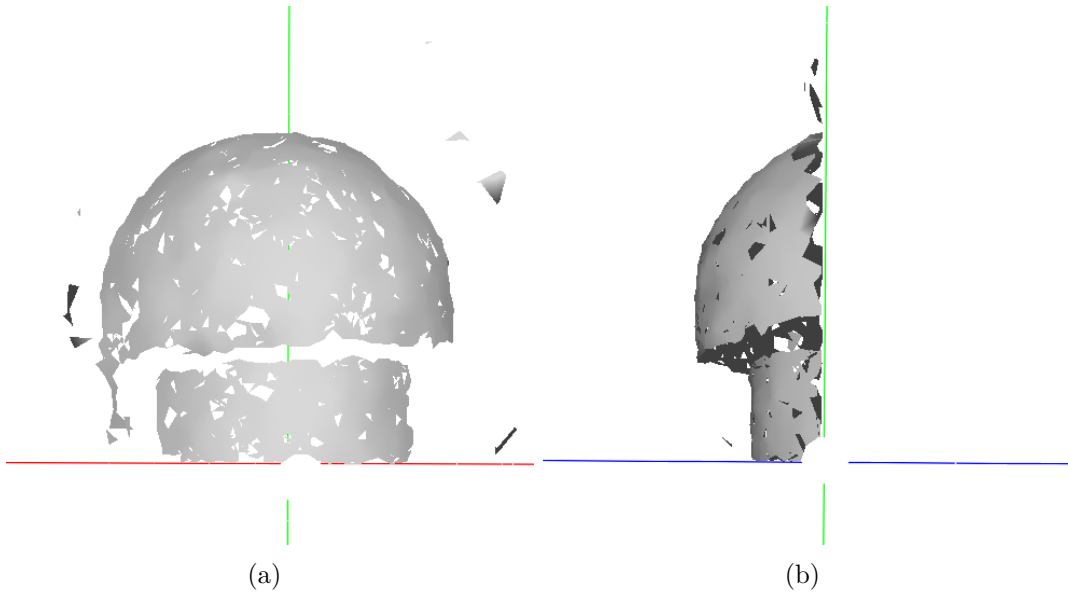
(a)        (b)

Figure 5.4: Reconstruction of the sample applying the solution of "asynch_pattern_search" method.



(a)        (b)

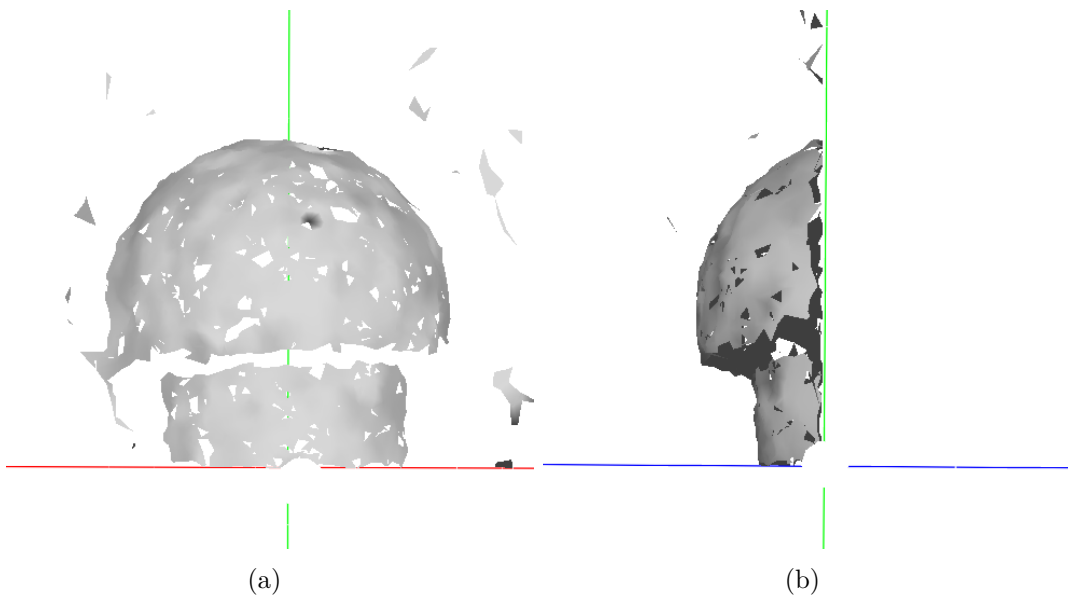Figure 5.5: Reconstruction of the sample applying the solution of "soga" method.

Finally, the intention is to reconstruct a similar object in two different positions with the same camera arrangement. Figures 5.6 and 5.8 are the pictures used as input of the reconstruction code. Also the input parameters used are the optimum obtained by the optimization algorithm in the conmin method case because it have the lowest

value of MSE.



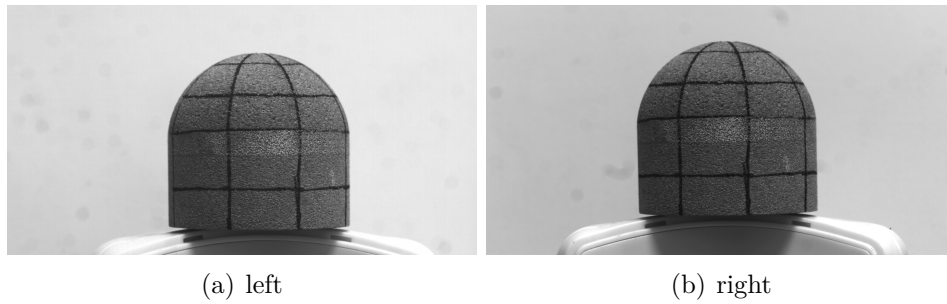(a) left          (b) right

Figure 5.6: Different geometry of cork sample used for the reconstruction
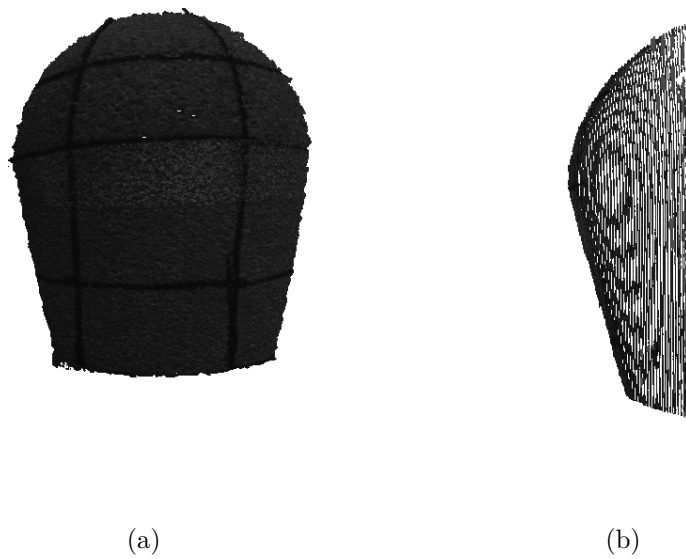


(a)          (b)

Figure 5.7: 3D point cloud of the reconstruction of the cork sample with the pictures of Figure 5.6.
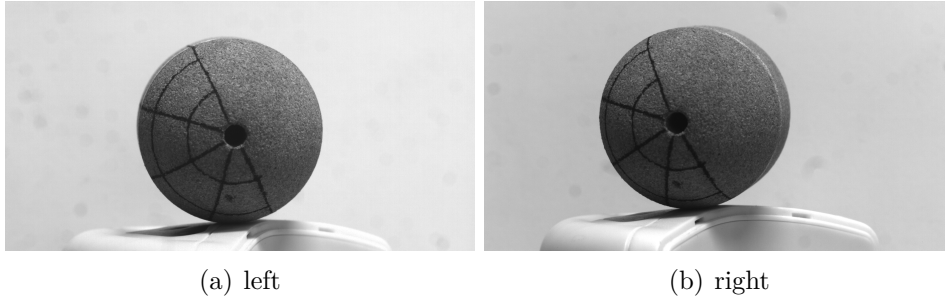
(a) left　　　　　　　　　　　　　(b) right

Figure 5.8: Different position of cork sample used for the reconstruction
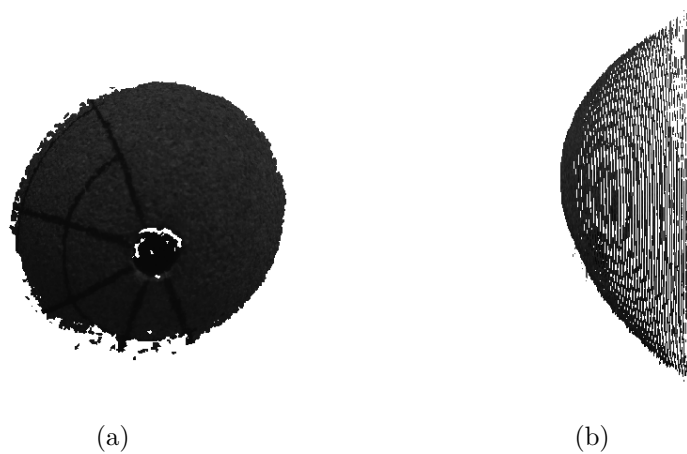


(a)　　　　　　　　　　　　　(b)

Figure 5.9: 3D point cloud of the reconstruction of the cork sample with the pictures of Figure 5.8.

Figures 5.7 and 5.9 show the reconstruction of the sample in the different positions. It can be seen that the first reconstruction is not as good as the previous cork sample used for the optimization algorithm because the bottom part of the reconstruction does not fit the cylindrical shape. However, the top of the sample can be seen that the shape fits the spherical shape in front and side views. In the second reconstruction the front view does not represent the whole shape of the hemisphere because there are not common points in this part. In the side view can be seen that the shape of the reconstruction conforms to the spherical part.

The main issues are the input parameters of the code because the values correspond to the other cork sample (Figure 5.2) so it is necessary to modify these values in order to adjust the reconstruction to the real shape. Moreover, it is possible that the common points in the pictures are not well recognized by the code because the features in

this kind of material (P50 cork) are not as visible as the other type of material (P45 cork).

# Chapter 6

# Conclusions and Future Work

## 6.1 Conclusions

With a specific arrangement of the cameras, that is, located horizontally and separated by a small angle, it has been possible to carry out the 3D reconstruction of the sample as seen at the end of the project. In addition, the optimization tool allows the user to find the optimal solution for a given geometry.

It was intended to use this procedure as a calibration method for other geometries but the result has been negative since an adequate reconstruction is not obtained. It is necessary to improve this technique in order to get better reconstructions.

The configuration used in the experiments of the VKI Plasmatron does not allow the reconstruction of the sample using the reconstruction code developed. The space limitation, and the position of the windows make difficult to find an optimum arrangement to take photos, with enough feature points easily to recognize by the code developed until now.

Regarding the quality of the pictures, the high brightness conditions and the short set-up time during the experiments have been a great inconvenience when taking photos with the desired quality during the experiments.

## 6.2 Future Work

As a future work, to carry out the 3D reconstruction of the sample during the experiments inside the VKI Plasmatron, it is proposed to find a fixed arrangement of the cameras in which the angle between them is less than 20 degrees. Then, identify the geometry to be able to adjust it to a mathematical function or a point cloud to apply the optimization algorithm developed. Once the optimal solution is found, these

parameters can be used to calculate the reconstruction of all samples with the same shape.

Furthermore, it is proposed to check if the code is able to identify distances, that is, due to the ablation of the materials during the experiments, the code must be able to measure the distance to a point on the sample and its time evolution.

Finally, to avoid the problem of overexposure, it is proposed to use gradual neutral density filters in order to reduce overexposure in the front sample area and not in the rear part that is not in these critical light conditions. This also allows the reduction of the f-number to reduce the depth of field and only have a focus of the sample.

# Chapter 7

# Budget

Tables 7.1 and 7.2 present a breakdown of the different costs of this project. The budget of this project only includes the cost of the personnel and the tests carried out in the VKI Plasmatron dedicated to this project. The cost of cameras, lenses, tripods, computers and other tools is not included. They have not been purchased for this project and had been previously amortized.

The cost of personnel is divided by the amount that I have received from the Erasmus internship scholarship, the cost of supervision of the VKI that includes one advisor and two supervisors and additionally the cost of the UPV supervisors who collaborate with this institution in the development of this project.

Finally, the cost of the experimental part includes only the tests performed with the P50 cork sample. The cost of the rest of the tests carried out are included in the budget of other projects.

The total cost of this project amounts to:

# Seven thousand and six hundred euros #

| Concept | Cost (€) |
|---|---|
| Engineer | 2100 |
| Advisor VKI | 1000 |
| Supervisor VKI | 2000 |
| Supervisor UPV | 500 |
| Experiments | 2000 |
| **TOTAL** | **7600** |

Tabla 7.1: Total cost of the project

| Concept | Units | Cost (€) |
|---|---|---|
| Test Plasmatron | 2 | 2000 |
| P50 Cork Sample | 2 | 0 |
| **TOTAL** | | **2000** |

Tabla 7.2: Operational cost associated to the VKI Plasmatron during the experiments.

# Bibliography

[1] Bernd Helber et al. "Material response characterization of a low-density carbon composite ablator in high-enthalpy plasma flows". In: *Journal of Materials Science* 49 (July 2014).

[2] *Xrays reveal how simulated atmospheric entry conditions impact spacecraft shielding.* https://newscenter.lbl.gov/2017/02/22/building-heat-shield-mars-mission/. Accessed: 2019-08-20.

[3] *Atmospheric Entry FX.* https://assetstore.unity.com/packages/vfx/particles/fire-explosions/atmospheric-entry-fx-148878. Accessed: 2019-08-20.

[4] Esper J. and Lengowski M. "Resin-Impregnated Carbon Ablator: A New Ablative Material for Hyperbolic Entry Speeds". In: (2012).

[5] Milos F. S. "Galileo Probe Heat Shield Ablation Experiment". In: *Journal of Spacecraft and Rockets* 34 (Dec. 1997).

[6] Loehle S. and Staebler T. "Photogrammetric Surface Analysis of Ablation Processes in High Enthalpy Air Plasma Flow". In: *AIAA Aviation* (June 2014).

[7] Schairer E.T. and Heinech J.T. "Photogrammetric Recession Measurements of Ablative Materials in the NASA Ames Sixty-Megawatt Arcjet". In: (Oct. 2003).

[8] Luhmann T. In: *Close Range Photogrammetry.* O'Reilly Media, 2011.

[9] Bradski G. and Kaehler A. "Projection and 3D Vision". In: *Learning OpenCV, 1st Edition.* O'Reilly Media, 2008. Chapter 12, pages 405–458.

[10] G. Martínez. "Development of a Photogrammetric measurement technique for the VKI Plasmatron". In: *RuiNet UPV* (Sept. 2018).

[11] F. Torres. "Thermal Characterization of Ablative Materials". In: (Feb. 2018).

[12] Georges Duffa. *Ablative thermal protection systems modeling.* American Institute of Aeronautics and Astronautics, Inc., 2013.

[13] Laub B. and Venkatapathy E. "Thermal Protection System Technology and Facility needs for Demanding Futures Planetary Missions". In: (Oct. 2003).

[14] Kolesnikov and Anatoli F. *Extrapolation from high enthalpy tests to flight based on the concept of local heat transfer simulation.* Technical report. Institute for Problems in Mechanics Moscow (USSR), 2000.

[15]  Teledyne Dalsa. *CCD vs. CMOS.* https://www.teledynedalsa.com/en/learn/ knowledge-center/ccd-vs-cmos/. Accessed: 17-08-2019. 2019.

[16]  Adimec. *CCD versus CMOS: Blooming and Smear Performance.* https://www. adimec.com/ccd-versus-cmos-blooming-and-smear-performance/. Accessed: 17-08-2019. 2019.

[17]  Cresta Project WordPress. *The Exposure Triangle.* https://light.elliottmccrory. com/. Accessed: 17-08-2019. 2019.

[18]  Intel Corporation. *Regions of Interest in Intel IPP.* https://scc.ustc.edu.cn/zlsc/ sugon/intel/ipp/ipp_manual/IPPI/ippi_ch2/ch2_regions_of_interest_in_ intel_ipp.htm. Accessed: 19-08-2019. 2019.

[19]  Cladera A. *La guía definitiva para exponer correctamente tus fotos.* https: //www.photopills.com/es/articulos/guia-exposicion. Accessed: 20-06-2019. 2017.

[20]  S.S. Cantos. "Desarrollo de Software para reconstrucción estéreo 3D". In: *RuiNet UPV* (Sept. 2019).

[21]  *Dakota.* https://dakota.sandia.gov/. Accessed: 2019-07-15.

[22]  Darrell D. "Fundamentals of Launch Vehicle Ablative Thermal Protection System (TPS) Materials". In: (2017).

[23]  Amorim Cork Composites. "Thermal Protection Systems". In: (2008).

[24]  CFOAM. *CFOAM® Carbon Foam Thermal Protection System (TPS) Applications.* http://www.cfoam.com/thermalprotection/. Accessed: 14-08-2019. 2019.

[25]  Reimer T. and Zuber C. "Determination of the Mechanical Properties of the Lightweigth Ablative Material ZURAM® ". In: (2003).

[26]  Allied Vision. *Installation Manual GigE Vision Cameras.* https://www. alliedvision.com/fileadmin/content/documents/products/cameras/various/ installation-manual/GigE_Installation_Manual.pdf. Accessed: 03-03-2019. 2015.

# Part I
# Appendix

# Appendix A

# Vimba Viewer User's Guide

There are two options to trigger the cameras. The procedure of both will be explained in the following sections.

## A.1   Trigger Over Ethernet

This Section consists of the explanation of the Trigger Over Ethernet Method carried out with the Vimba Viewer Software. This methods is simple to use but the cameras are not synchronized with the other measuring devices.

First of all, when the software is open, the main window show the cameras which are connected to the computer (Figure A.1). In thit case, the camera models are GT2000 and GT2050 as explained before.

The next step is to open the configuration window of both cameras pressing the white box (Figure A.2 in order to set the cameras.

Then, there is a principal window where the camera image will appear. For that, once the exposure time is set according to the light conditions, pressing the button on the upper left part of the window, the camera will start to grab.

An important step is to configure the frame rate of the camera because in this application is important to have the same value in both cameras. For that in the last tab *All* can be found this option.

When a multiple camera is connected, the *StreamBytesPerSecond*. It can configured as Figure A.6 shows. The maximum value can be calculated according to the Equation (A.1). The total should not exceed the maximum value of the bandwidth which is calculated according to the Equation (A.2).
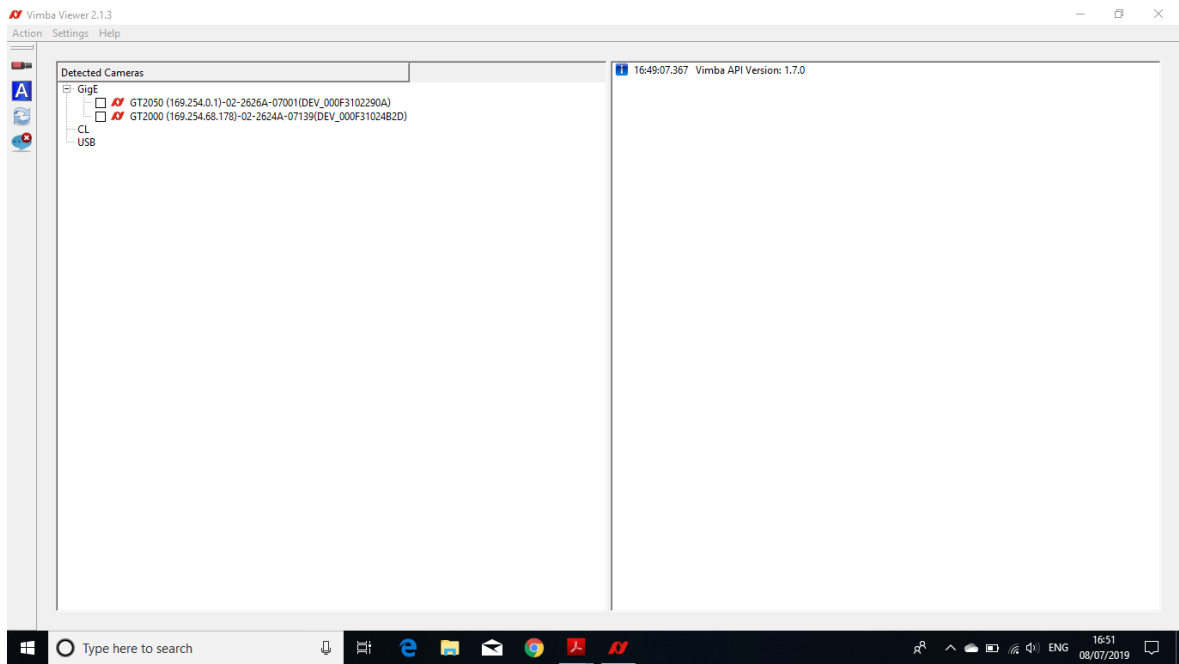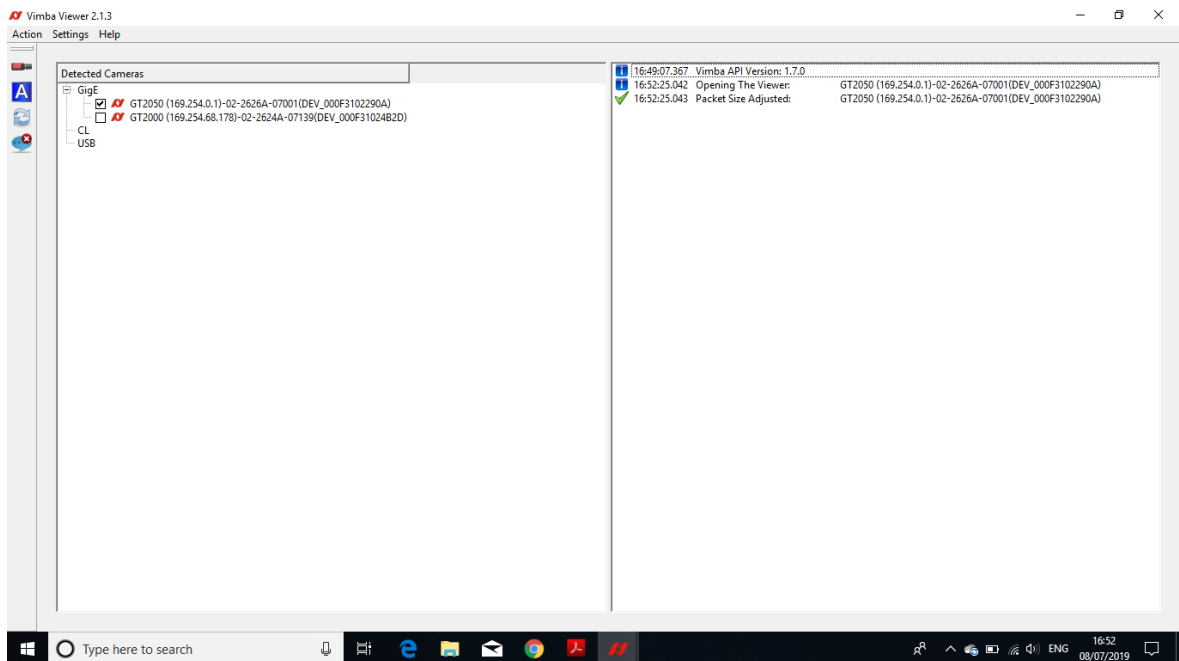
Figure A.1: Step 1: Main window of the software.



Figure A.2: Step 2: Opening the configuration window of the cameras.
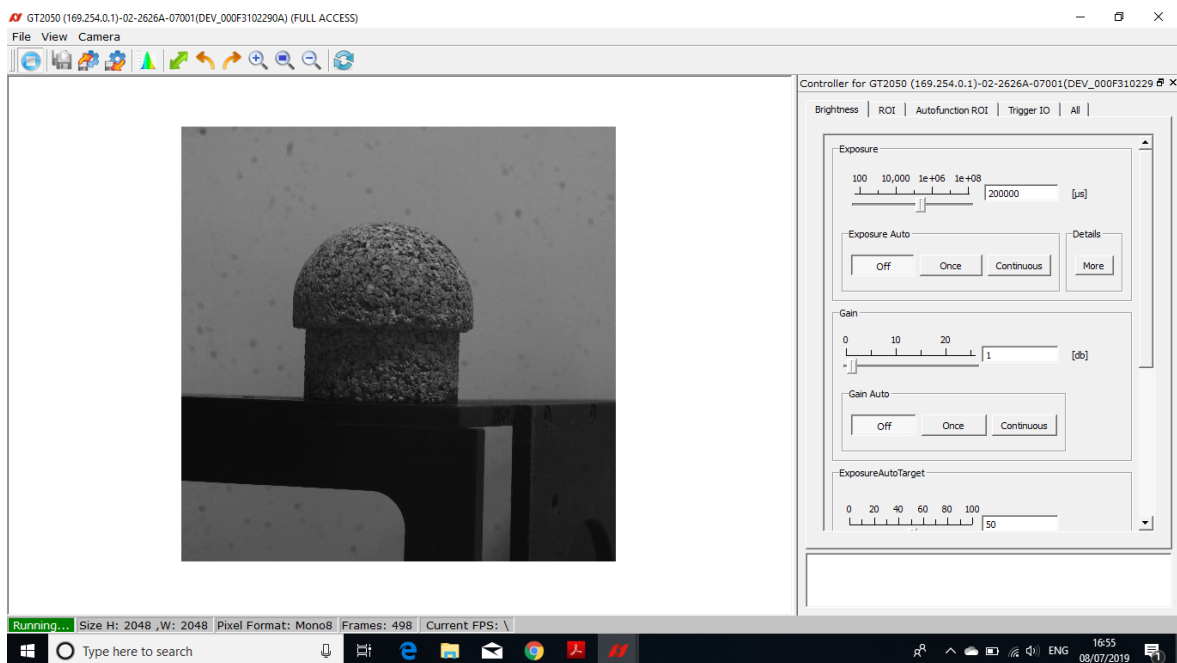
Figure A.3: Step 3: Main window prepared to visualize the camera image.



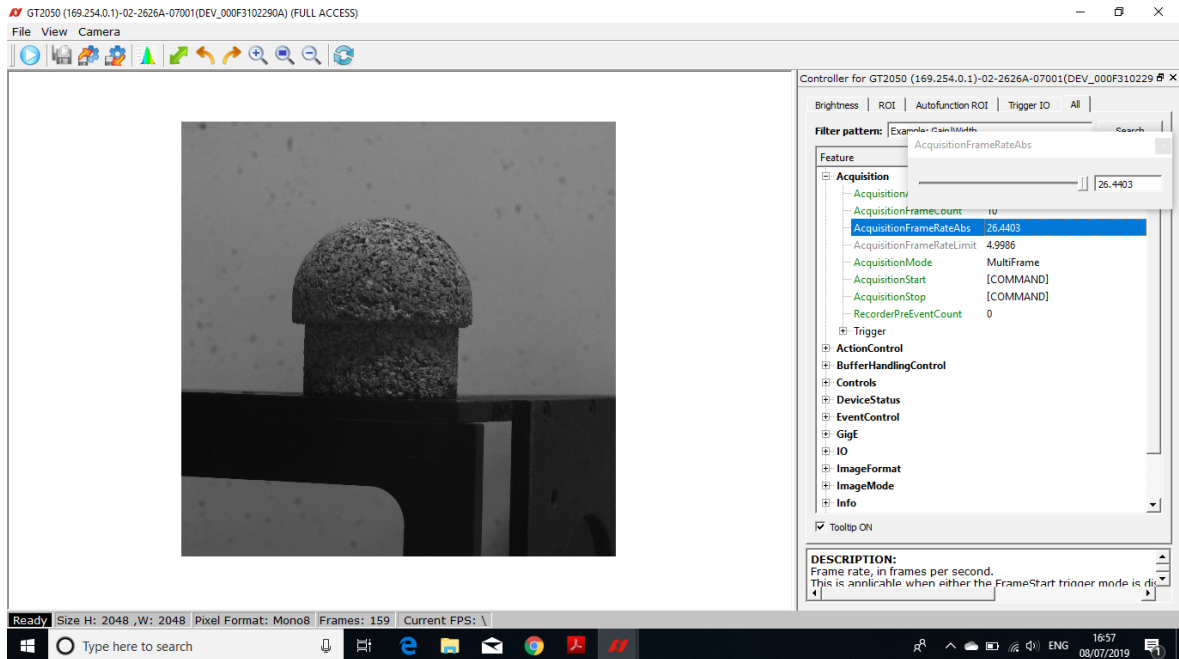Figure A.4: Step 4: Camera grabbing

Figure A.5: Step 5: Change the Acquisition Frame Rate
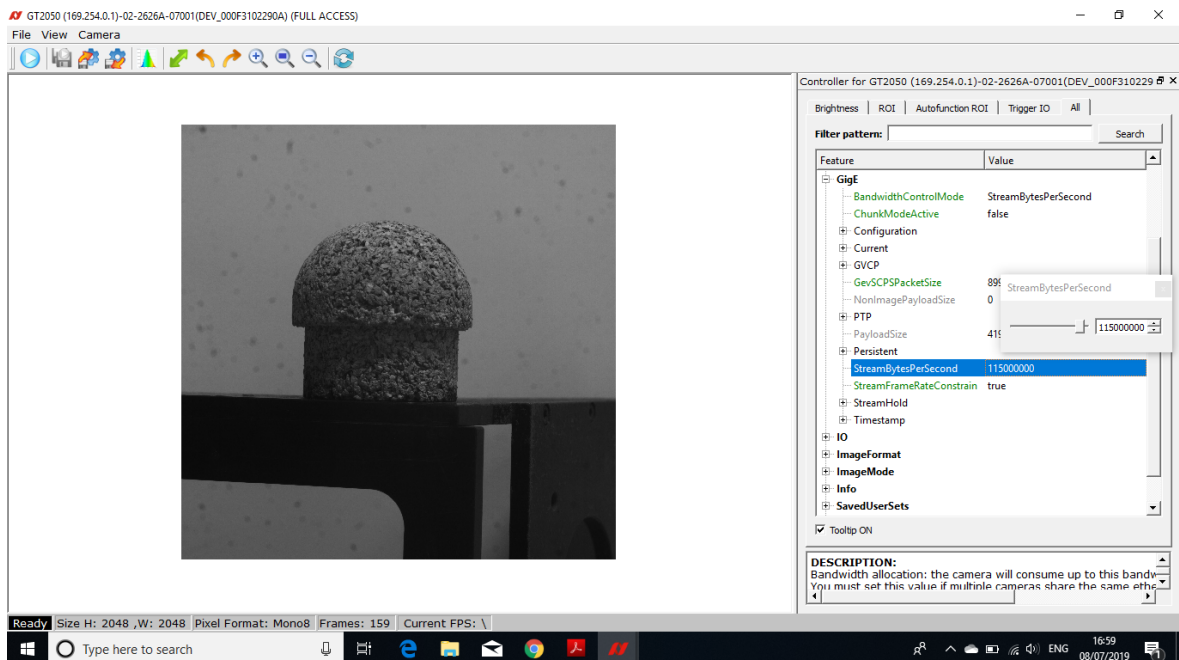


Figure A.6: Step 6: Configuring the maximum Stream Bytes Per Second according to the Bandwidth

$$StreamBytesPerSecond = Height\ x\ Width\ x\ FrameRate\ x\ Bytes\ per\ Pixel \quad (A.1)$$

$$Bandwidth = Width\ x\ Height\ x\ BytesPerPixel\ x\ FrameRate\ x\ Number\ of\ Cameras = $$
$$Value\ in\ MBps\ (Megabytes\ per\ second)$$
$$(A.2)$$

Once the camera settings are established the procedure to trigger the cameras to start recording pictures begins as follow. Action Control needs to be configured with the numbers as is showed in Figure A.7.
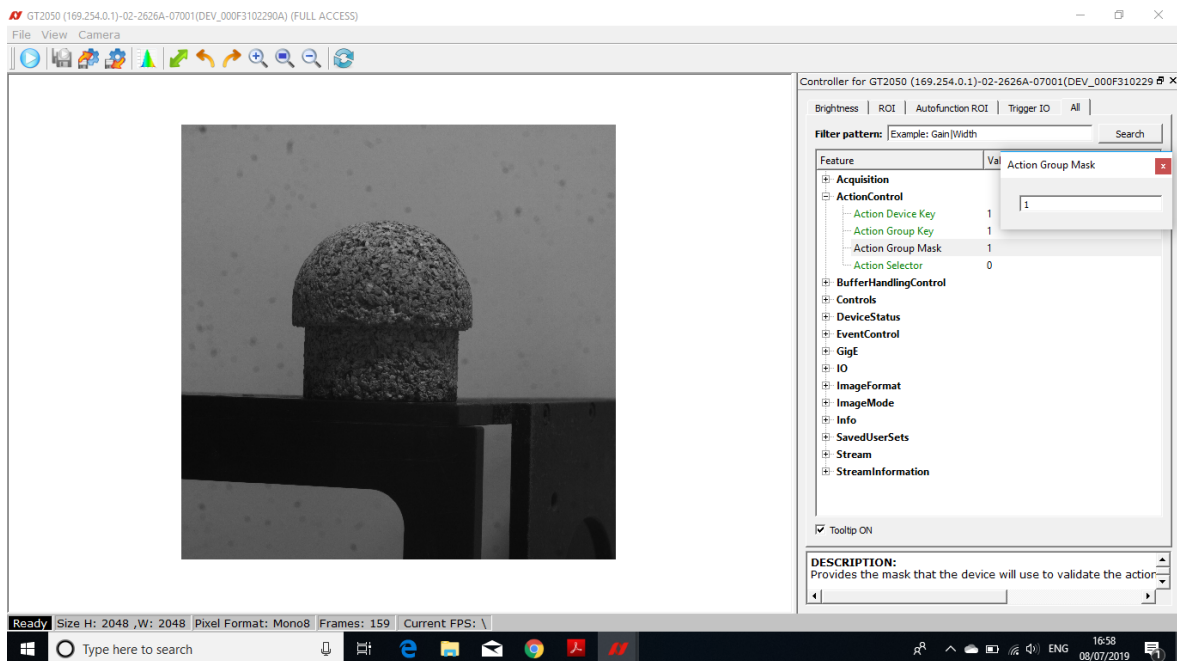


Figure A.7: Step7: Configuring the numbers of the Action Control to start the process of Triggering

Then in the *Trigger IO* tab, the first step is to press the *Bulk* button. Then, all of the gaps need to be configured as Figure A.8. The next step, in the *File* button placed on the upper left, select the option *Image Series Option*.

The following window appear with the saving options (Figure A.9. The number of pictures to save, the format of the picture and the name of the picute can be changed by the user. Finally, the last step is to press the button next to the *Play* button which the camera will be ready to start recording pictures.
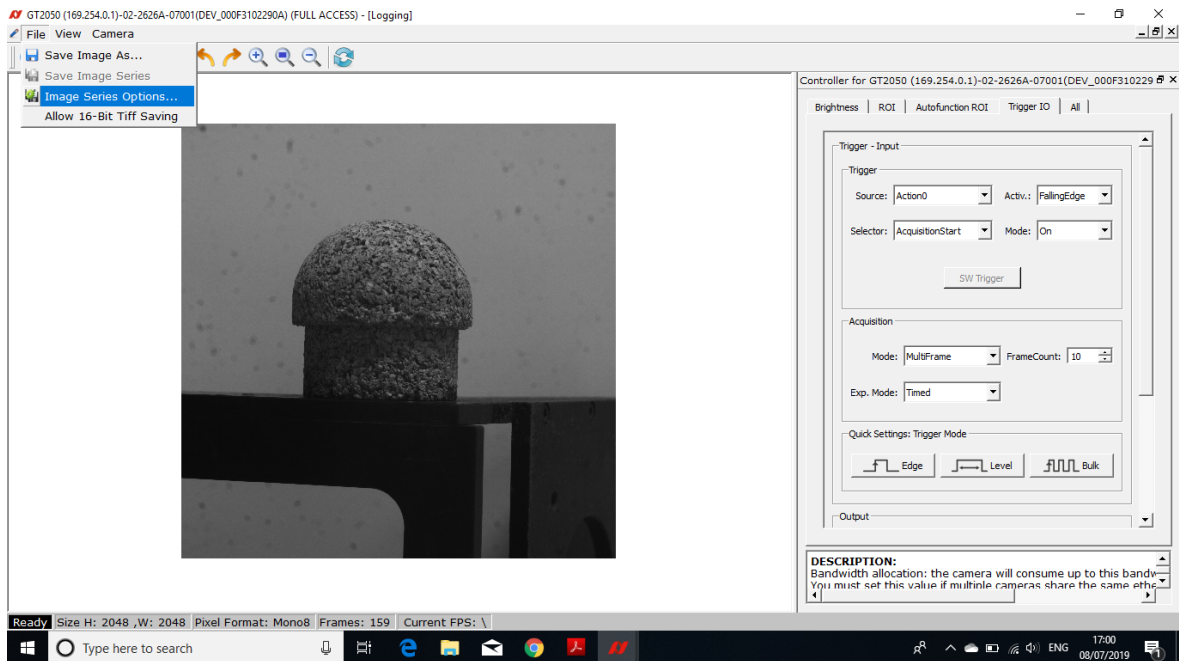
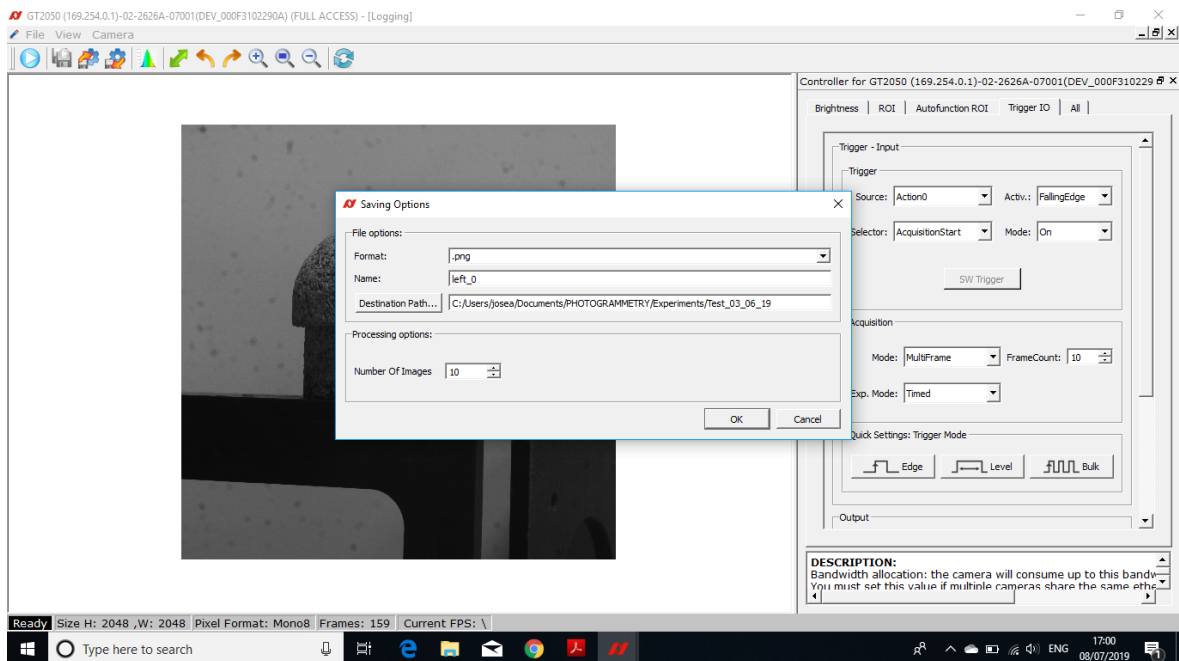Figure A.8: Step 8: Characteristics of the Triggering Process



Figure A.9: Step 9: Saving options of the pictues

In the main window, when the user press the *A* blue button on the upper left, the window of the Figure A.10 appears and the gaps of Action Command need to be filled with the same numbers as the *Action Controls*.
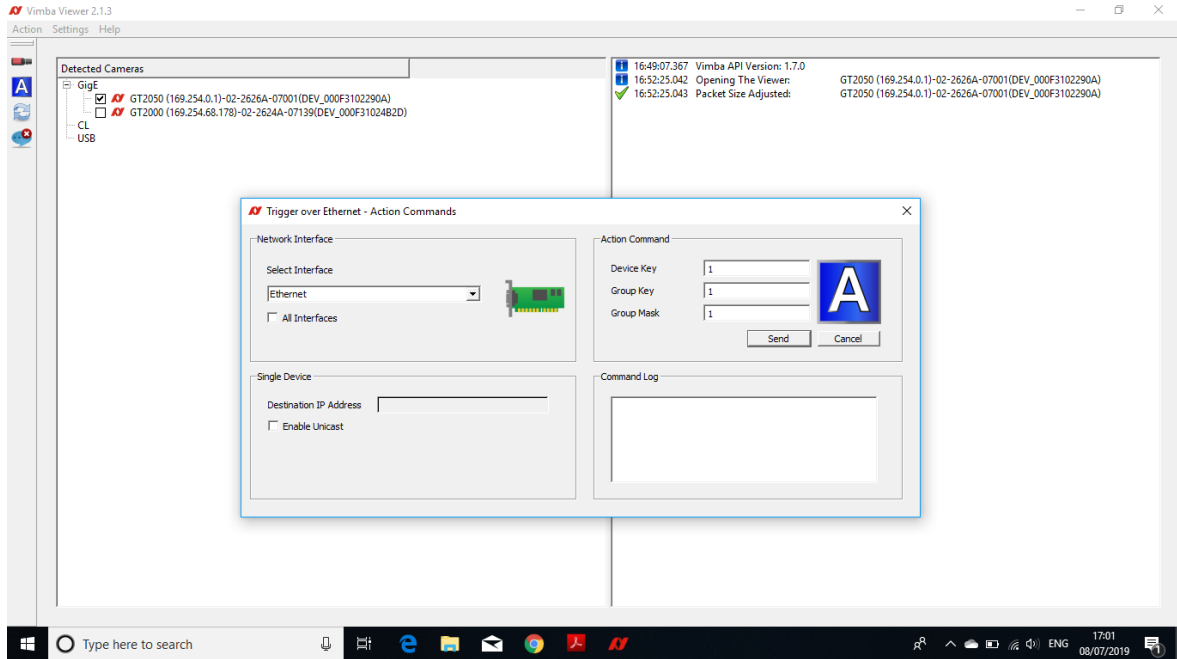


Figure A.10: Step 10: Window to send the Action Commands and starting the process of recording pictures

Finally, the recording process will start and a window will appear with the Saving Process (Figure A.10.)

Figure A.11: Step 11: Saving the pictures

## A.2   External Trigger

Figure A.12 shows the scheme of the pins and cables necessary to the external trigger with a signal generator. This is an alternative method to trigger the cameras and synchronize them with the other measuring devices during the ablation experiments.

## EXTERNAL TRIGGER FOR PROSILICA GT CAMERAS
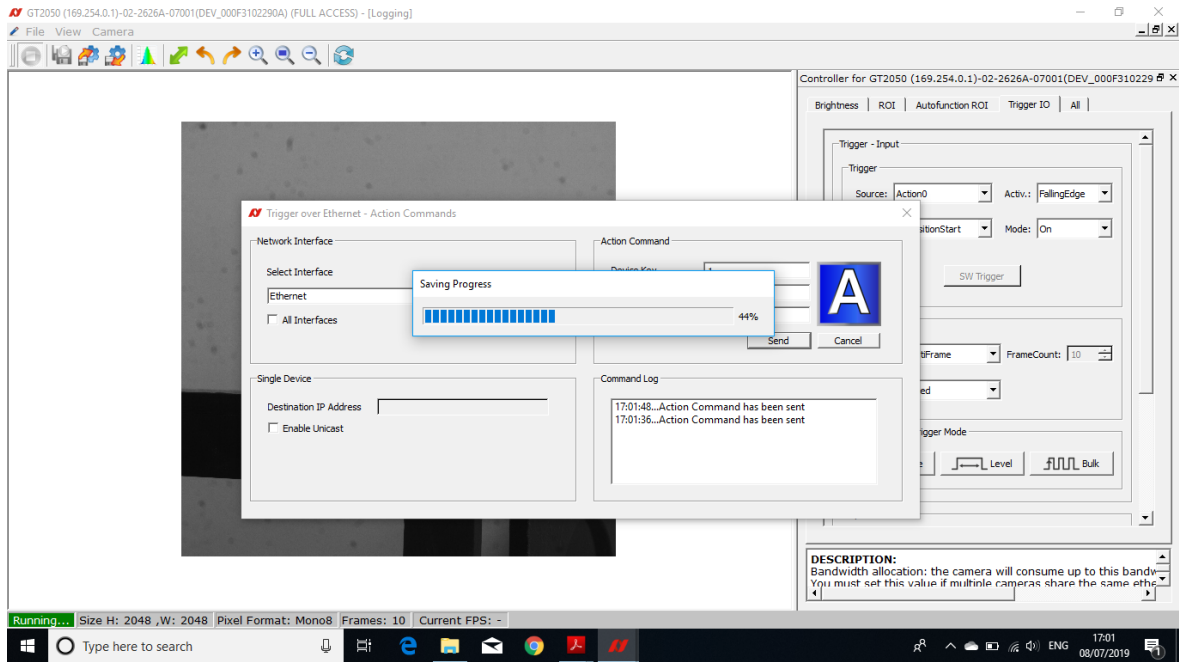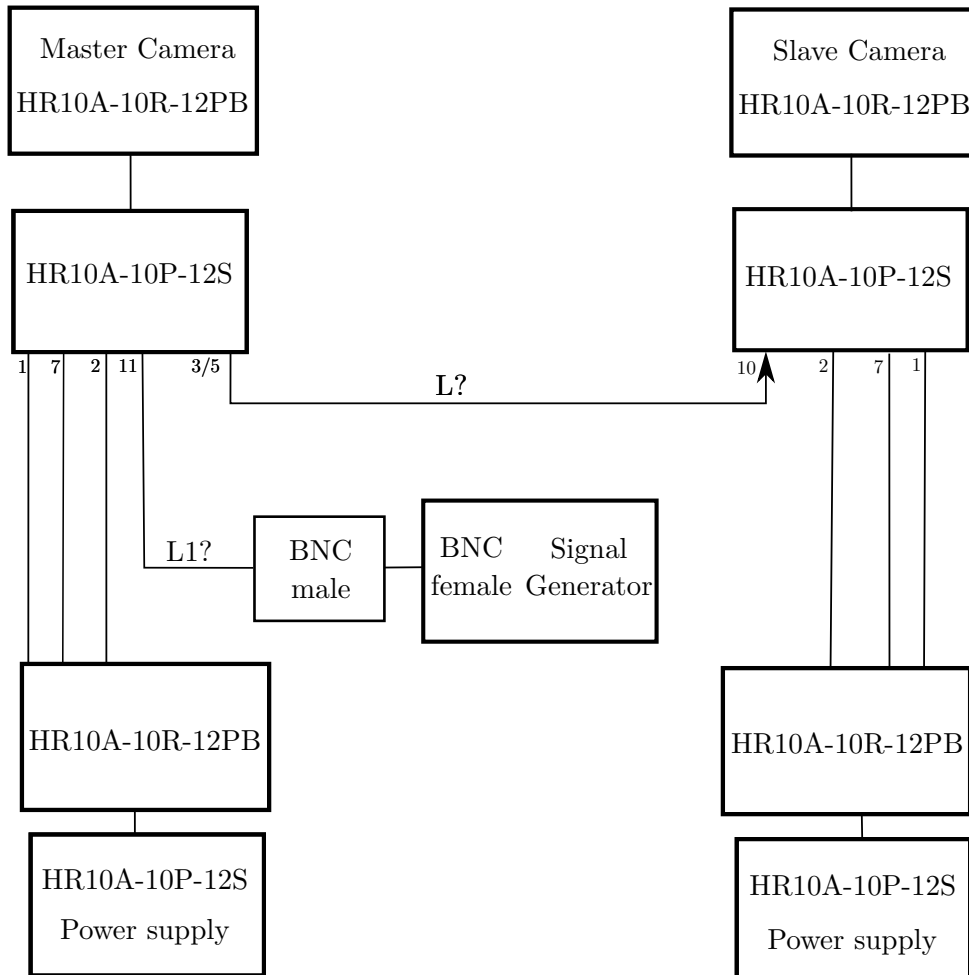
```
┌──────────────────┐                    ┌──────────────────┐
│  Master Camera   │                    │   Slave Camera   │
│ HR10A-10R-12PB   │                    │ HR10A-10R-12PB   │
└──────────────────┘                    └──────────────────┘
         │                                       │
┌──────────────────┐                    ┌──────────────────┐
│                  │                    │                  │
│ HR10A-10P-12S    │                    │ HR10A-10P-12S    │
│                  │                    │                  │
└──────────────────┘                    └──────────────────┘
 1  7  2  11  3/5          L?          10   2   7   1
```

Pin assignment:

- Pin 1: Ground
- Pin 2: Camera power supply
- Pin 3/5: Opto-isolated Output
- Pin 7: Isolated input signal ground
- Pin 10: Power input for opto-isolated outputs
- Pin 11: Input 2 opto-isolated

Material needed:

- 2 x Hirose HR10A-10R-12PB (12 pin male)

- 2 x Hirose HR10A-10P-12S (12 pin female)

- 1 Male BNC connector

- Cable L1: depends on the position of the master camera

- Cable L: depends on the relative position of the cameras (3 m) aprox.

82

Figure A.12: Scheme of the External Trigger

# Appendix B

# Frames and Videos with Python

```python
#import numpy as np
import cv2

# Opens the Video file
cap= cv2.VideoCapture('Video6.avi')
path = 'C:/Users/josea/Documents/PHOTOGRAMMETRY/Experiments/
    Test_14_05_19/Test_JAI/Video6/'
i=0
while(cap.isOpened()):
    ret, frame = cap.read()
    if ret == False:
        break
    cv2.imwrite(str(path) + 'frame' + str(i)+'.png',frame)
    i+=1

cap.release()
cv2.destroyAllWindows()
```

Listing B.1: Extrat frames from a video with Python

```python
import cv2
import numpy as np
import glob


img_array = []
for filename in glob.glob('C:/Users/josea/Documents/PHOTOGRAMMETRY/
    Experiments/Test_14_05_19/Test_4/left/*.bmp'):
    img = cv2.imread(filename)
    height, width, layers = img.shape
    size = (width,height)
    img_array.append(img)
#    print(filename)



out = cv2.VideoWriter('project.avi',cv2.VideoWriter_fourcc(*'DIVX'),
    5, size)
```

```
16
17 for i in range(len(img_array)):
18     out.write(img_array[i])
19 out.release()
```

Listing B.2: Create a video from frames with Python